UNIVERSITEIT VAN PRETORIA
UNIVERSITY OF PRETORIA
YUNIBESITHI YA PRETORIA

Diffusion of ion implanted iodine in 6H-SiC

by

Remeredzai Joseph Kuhudzai

Submitted in partial fulfillment of the requirements for the degree of

MAGISTER SCIENTIAE

in the Faculty of Natural and Agriculture Sciences at the University of Pretoria

July……2010

Supervisor/Promoter: Prof. J.B. Malherbe

Co-supervisor: Prof. E.K.H. Friedland

SUMMARY

The diffusion of iodine implanted 6H-SiC has been investigated using Rutherford backscattering Spectrometry (RBS). SiC is used as the main barrier in the modern high temperature gas cooled reactors. An understanding of the transport behaviour of iodine in 6H-SiC will shed some light into SiC's effectiveness in the retention of fission products. Room temperature iodine implantations were performed to a fluence of 1×10^{16} iodine ions per cm^2. Iodine depth profiles were determined by Rutherford backscattering spectroscopy. Previous studies indicate that iodine diffusion cannot be detected for temperatures below 1000°C. Isochronal annealing experiments for 5 hours cycles were then performed starting from 1000°C. 5 hour annealing cycles at 1200°C and 1300°C were also performed. These relatively short annealing cycles were used to study the evolution of the iodine depth profiles and to determine the temperature where the first noticeable broadening of the iodine implanted profile is observed.

Broadening of the iodine profile was initially observed at temperatures around 1200°C. Isothermal annealing cycles were then performed at this temperature of 1200°C where the broadening was first observed. The annealing experiments were performed for a total annealing time of 60 hours. Isothermal annealing experiments were also performed at a lower temperature of 1100°C also for a total annealing time of 60 hours. The experimental data was analyzed by fitting the iodine depth profiles to a Gaussian function using the GENPLOT program.

Diffusion coefficients were obtained by comparing the full widths at half maximum, (FWHM) of the iodine profiles before and after annealing. Results for 1100°C show that the diffusion coefficient is below 10^{-21} m^2 s^{-1}. Solving the diffusion equation numerically for this diffusion coefficient shows that the iodine does not traverse more than 2 µm through SiC after annealing for one year. Intact SiC coatings which have a thickness of 35 µm in the fuel particles will therefore be able to prevent iodine release from the particle at this temperature. Results for 1200°C show that the diffusion coefficient is in the order of 10^{-20} m^2 s^{-1}. The results also reveal that iodine loss through the front surface is relatively low with only 15% of iodine loss observed after annealing for a total time of 60 hours. Further indications of SiC ability to retain iodine are observed when an iodine peak is still present after annealing for 30

hours at a temperature of 1500°C. Radiation damaged produced during ion implantation was investigated by Rutherford backscattering in conjunction with channeling. The results of the RBS/channeling reveal that the room temperature implantations produce an amorphous layer from the surface up to a depth of 260 nm. Some epitaxial regrowth is observed starting at approximately 1000°C.

DECLARATION

I, Remeredzai Joseph Kuhudzai declare that the dissertation, which I hereby submit for the degree of MSc in Physics at the University of Pretoria is my own work and has not previously been submitted by me for a degree at this or any other tertiary institution.

Signature: ……

Date: ……

Acknowledgements

I would like to acknowledge the following people for their support in making this study a success.

- My academic promoter, Prof. J.B. Malherbe, my co-promoter Prof. E. Friedland, Dr. N.G. van der Berg, and Prof. C.C. Theron for their wonderful guidance and mentorship during this study.

- The head of department, Prof. J.B. Malherbe and Prof H. Alberts, for arranging some part-time work in the department which helped my finances during my study.

- Ms Elfreida Meyburgh and Mr. Gerhard Pretorius for all the assistance in the Physics department.

- Dr E. Wendler and colleagues from Jena, Germany.

- Fellow students in the physics department, Thulani, A. Chawanda, W. Mtangi, H. Gavi, Mxolisi, Thoko, Prime and C. Nyamhere for their encouragement and moral support.

- All my best friends and Tendo, for all the love.

- My brothers, my sister and her husband, my sister in laws and my nieces for their love and support.

- My late parents for giving me a great foundation to be who I am today, and my late brother Farikai for being a loving brother and mentor.

Contents

Chapter 1: Introduction

1.1The Pebble Bed Modular Reactor (PBMR)

Nuclear reactors are expected to play a major role in meeting the world's ever increasing energy demands. The decreasing supply of fossil fuels and the need to reduce green house gas emissions are the major factors influencing this renewed drive for the development of alternative energy sources. High Temperature Gas Cooled Reactors (HTGR's) are being considered for electricity generation and for process heat applications such as high temperature electrolysis for the production of hydrogen by water splitting as opposed to the conventional production of hydrogen from hydrocarbons.

The HTGR uses coated fuel particles to permit high outlet coolant temperature. The helium coolant gas and the graphite, employed as a moderator, offer enhanced thermal and neutron efficiency respectively [Eld09]. The Pebble Bed Modular Reactor, (PBMR) proposed as the HTGR for South Africa, uses the Tri-Isotropic (TRISO) particle design consisting of a (UO_2) fuel kernel surrounded by successive layers of a low density pyrolytic carbon, a high density pyrolytic carbon, silicon carbide (SiC) and an outer layer of high density pyrolytic carbon [Sch90]. The porous carbon buffer layer is designed to protect the inner pyrolytic carbon layer from damage by recoiling fission fragments from the kernel. It contributes voids to compliment the voids contained in the fuel kernel to capture gasses created by the fission process, thereby reducing the pressure exerted on the denser inner pyrolytic carbon. The inner pyrolytic carbon acts as a barrier for gaseous fission products and reduces tensile stress in SiC layer [Han03]. The SiC layer in between the two high density pyrolytic carbon layers is considered the main barrier to fission product release, especially for metallic fission products. The outer pyrolytic carbon layer protects SiC layer from possible external mechanical and chemical interactions or attacks. It also helps to reduce tensile stress in the SiC [Nic02].

Commissioning of the HTGR's will depend on their ability to retain the radioactive fission products. Fission products not retained are transported from their original fission sites through the fuel material to the surface of the coated spheres where they are desorbed into the coolant gas or plate out onto the cooler surfaces of the primary circuit, like the colder parts of the steam generator. The released fission products pose a risk to people who access the main power system for maintenance purposes and increase the demands for decontamination of the plant. Inhalation, ingestion and absorption are the major potential exposure pathways of the radiation. The levels of exposure could be increased in accident conditions. A depressurization accident results in loss of the contaminated primary coolant to the atmosphere and a water ingress accident will remobilize the fission products that would have plated out, (deposited) on the components of the primary coolant circuit by scrubbing of water and steam [Yua02]

The structure of the TRISO particle is shown in Fig. 1.1

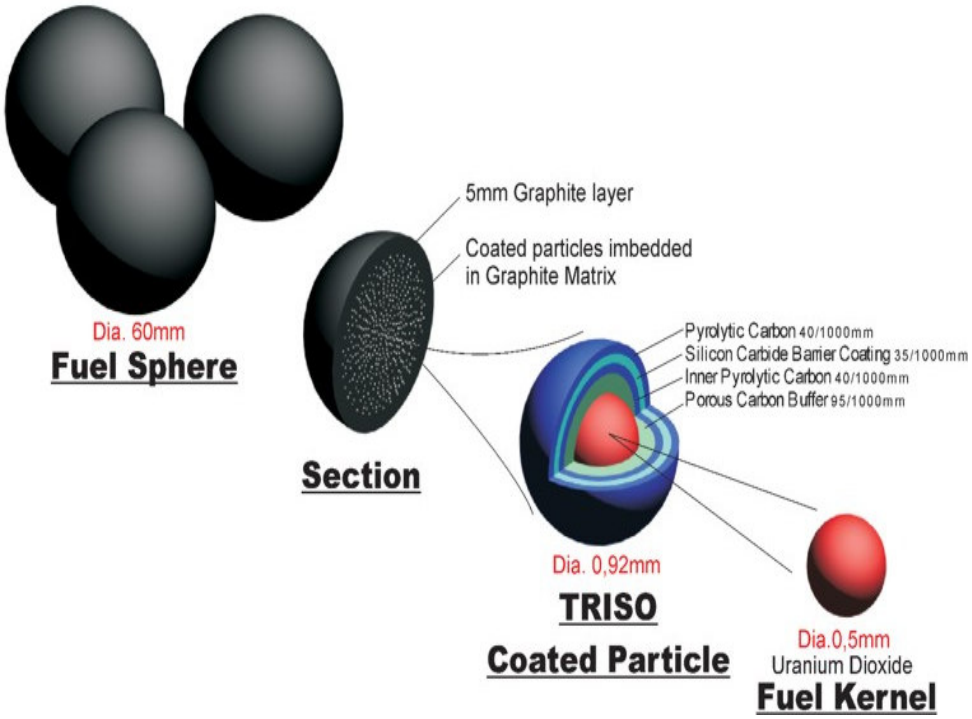

Figure 1.1: Schematic diagram of fuel for a pebble-bed modular reactor. Taken from [www1].

1.2 Silicon Carbide (SiC)

The choice of silicon carbide, (SiC) as the main barrier to the fission products is influenced by its exceptional mechanical properties and its ability to retain these properties at high temperatures. SiC is one of the hardest materials known with a Mohs hardness of around 9.5. The hardness is due to a high bond strength resulting from the short bond length between Si and C which is about 1.89 Å [Zso05]. SiC has a high corrosion resistance and also good resistance to chemical and abrasive attack. It has a high thermal conductivity which allows for lower operating fuel temperature. SiC's appeal is also strongly influenced by its low neutron absorption cross section. Perhaps the most important feature of SiC that supports its case as the main barrier to fission products in the TRISO particle is its high thermal stability. SiC maintains its outstanding mechanical properties at high temperatures above 1000°C [Pir93]. The temperature of modern HTGR's under normal operation average around 950°C. The core temperature does not exceed 1600°C [Moo08] in case of core heat up events. SiC sublimates at temperatures around 2800°C [Zso05, Wol05], however, other authors note that SiC melts at around 2700°C [Wan08] and others have noted that SiC is already decomposing at around 1500°C into Si, C, SiC_2 and Si_2C [Lil93]. Therefore SiC should in principle be a reliable barrier to fission products during the operation of the reactor under normal operating conditions of around 900°C.

The structure of SiC can be considered to be an assembly of tetrahedra [Pir93, Sne07], with two neighbouring tetrahedra, joined together at their corners. The mostly covalent bonded tetrahedron, can take any of the two forms SiC_4 or CSi_4 as shown in Fig. 1.2 [Zso05]. A silicon atom can be at the center of the tetrahedron surrounded by four carbon atoms or a carbon atom at the centre of the tetrahedron surrounded by four silicon atoms. The angle Θ shown in Fig. 1.2 is approximately 109° and the angle between two faces in the tetrahedral is approximately 70° [Bra88, Zso05].

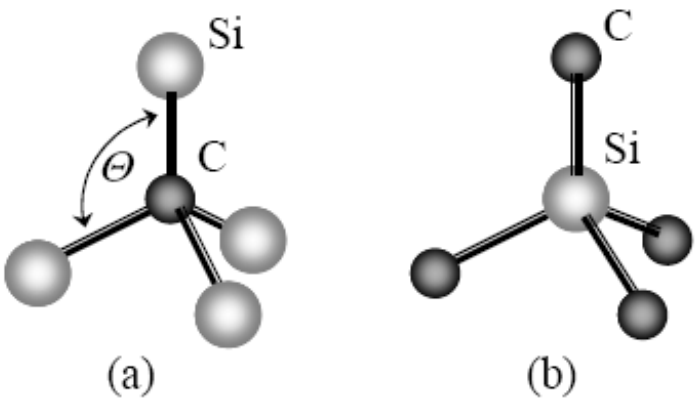

Figure 1.2: Tetrahedra showing (a) one carbon and four silicon atoms (b) one silicon and four carbon atoms. Taken from [Zso05].

A difference in the stacking sequence of identical atomic planes along a principal crystallographic and a large number of possible combinations of this stacking sequence, result in silicon carbide exhibiting a phenomenon known as polytypism. SiC is known to have over 200 polytypes [Dev00]. The Ramsdell notation is widely used to describe the polytypes [Zso05]. The Ramsdell notation uses a number followed by a letter to prefix acronym SiC. The number represents the count of double layers in one period and the letter defines the symmetry with the more common letters, C and H standing for Cubic and Hexagonal respectively. Only one cubic polytype, 3C-SiC is known and the most common hexagonal polytypes are 4H-SiC and 6H-SiC [Dev00]. In this work we have used 6H-SiC wafers supplied by Cree Inc®. Cree Inc® uses the Modified Lely Method to prepare the wafers.

1.3 Radiation damage in SiC

In this work, in order to investigate the effectiveness of SiC in retaining the fission products, ions of one of the significant fission products, iodine, were implanted in SiC. The production of radiation damage and the diffusion behaviour of the iodine were then analysed. Studies by McHargue *et al,* [McH93], show that SiC is easily amorphized by ion implantation of low energy ions, in the order of a few hundred keV at room temperature irrespective of the ions implanted. They further state that the accumulation of the radiation damage is approximately linear with fluence until amorphization occurs. Wesch *et al* [Wes95] implanted 230 keV Ga^{+} ions at various fluences and temperatures into SiC. Their investigations show that amorphisation is reached at -193°C for fluences above 1×10^{-14} cm $^{-2}$. At a temperature of 27°C, their studies show that amorphisation is reached for fluences between 2×10^{14} cm $^{-2}$ and 3×10^{14} cm $^{-2}$. Wesch et al also found that for implantation temperatures around 300°C amorphisation is avoided up for fluence up to 1×10^{16} cm $^{-2}$. Higher temperatures are required to avoid damage for fluences higher than 1×10^{16} cm $^{-2}$.

On the aspect of annealing of the damage, McHargue *et al*, find that for low damage, when an amorphous surface region is not produced, the damage anneals in the temperature range of 200°C to 1000°C. However, for the amorphous scenario, the regrowth is less clear and the ranges are from 750°C to 1700°C. Audren *et al*, [Aud07] observed that SiC is also easily amorphised by 300 keV Cs ions. At a fluence of 6 x 10^{14} cm^{-2} Cs ions, their studies show an amorphous layer extending to a depth of approximately 150 nm below the surface. Their Rutherford Backscattering combined with channeling (RBC/C) studies reveal that annealing of the damage begins at around 600°C, starting from the interface between the damaged layer and the crystalline bulk. They only start to see some appreciable recystallisation at temperatures above 960°C, with roughly 50% of the damage annealed at approximately 1300°C.

Wendler *et al*, [Wen98], implanted antimony ions to a fluence of 3 x 10^{14} cm^{-2} at energy of 300 keV. They also observed some recystallisation starting to occur at an annealing

temperature of 950°C for a period of 30 s. They reported an apparent perfect recystallisation of the amorphous layer for a 1500°C annealing cycle for 60 minutes in argon ambient, however, they also note that the amorphous layer could have been etched away as they no longer observe the implanted ion profile after the annealing cycle. Similar results were obtained for iodine ion implantation in SiC to fluence of 2.7 x 10^{14} cm^{-2} Audren *et al* [Aud08]. An amorphous layer initially extending to a depth of 250 nm, showed some appreciable recystallisation on annealing at a temperature of 1000°C. Results from these three studies seem to suggest that the recystallisation of the amorphous SiC starts around 900°C. Annealing temperatures ranging from 850°C to approximately 900°C are required to transform disordered Si-C bonds into the ordered 3C-SiC structure [Wes96].

1.4 Radiological significance of Iodine

Iodine is known to accumulate in the thyroid gland. Exposure to the radioactive iodine isotopes could lead to thyroid cancer and therefore the extent to which the SiC retains the fission product iodine is essential to the development of HTGR's. There are two radio-active iodine isotopes. One of the isotopes is ^{131}I which has a half life of about 8 days. This half life is fairly short, however, the more significant property of the isotope is its biological half life which is approximately 140 days. ^{129}I, is the other isotope and has a half life of 15 million years. These isotopes could be produced by the following possible fission reactions:

$$^{235}U + n \rightarrow {}^{236}U \rightarrow {}^{129}I + {}^{107}Y \qquad (1.1)$$

$$^{235}U + n \rightarrow {}^{236}U \rightarrow {}^{131}I + {}^{105}Y \qquad (1.2)$$

where the uranium ^{235}U nucleus, absorbs a neutron giving rise to the highly unstable ^{236}U nucleus. The unstable uranium nucleus then undergoes fission, splitting into two fragments. In equation 1.1, the fragments are the isotopes ^{129}I of iodine and ^{107}Y of

Yttrium. In equation 1.2, the resulting fragments are ^{131}I of the iodine and ^{105}Y of Yttrium.

1.4.1 Diffusion of iodine in SiC

In literature, not much is known or has been published, with regards to the diffusion behaviour of iodine in SiC. Investigations by *Audren et al*, [Aud08], for 700 keV, iodine ion implantation at room temperature, reveal that the iodine profile from RBS spectra does not change even after annealing up to a temperature of 1000°C for 30 minutes. 1000°C is the typical maximum temperature of the UO_2 kernel during normal operation of the HTGR. They conclude that they could not detect any diffusion of the iodine in SiC up to a temperature of 1000°C and that this would suggest that SiC could potentially be an adequate barrier to the fission product iodine. However, isotopes of the fission product iodine are known to accumulate in the primary coolant circuit during normal operation and can become significant under accident conditions [Han03]. Data on the release of the potentially hazardous fission products has been compiled from research carried out over a period of about 40 years on prototypes of the HTGR like the Dragon reactor (UK), Peach Bottom1 (USA) and the Arbeitsgemeinschaft Versuchsreaktor, more commonly known as the AVR (Germany).

Gottaut *et al*, [Got90] carried out some experiments at the German pebble bed reactor, the AVR. They sampled coolant gas in hot and cold loops they called VAMPYR I and VAMPYR II respectively and their results revealed that significant amounts of iodine isotope ^{131}I, where present in the primary coolant gas. Specific activities of ^{131}I were in the order of 5, 2 $x10^2$ Bq/m^3. Results from irradiation experiments on fuel elements carried out in a materials test reactor by A. Christ and W. Schenk [Chr85] are in agreement with those from the AVR experiments. Borisov *et al*, [Bo94], used carbon filters with silver nitrite to trap the fission iodine at the exit channel of the helium of their experimental apparatus. They found that radioactive iodine isotopes ^{131}I and ^{133}I produced in irradiated fuel elements were present in the helium in the form of aerosols and gas.

1.5 Outlay of this dissertation

The fact that iodine isotopes have been found in the primary coolant circuit warrants further investigation of the behaviour of iodine in the main barrier to the fission products, SiC. In our work, we try to shed some light into the diffusion behaviour of implanted iodine at temperatures above 1000°C. We also investigated the damage created by implantation of iodine at room temperature and the annealing of this damage at temperatures above 1000°C. Rutherford backscattering spectrometry, RBS, and α-particle channeling were the main analytical techniques used in our research. In chapter 2, we discuss the theory of diffusion. Chapter 3 gives a brief description of ion-solid interactions with particular emphasis on ion implantation. The theory of RBS follows in chapter 4. Experimental details are outlined in chapter 5. In chapter 6, we present our results. The summary and conclusion follow in chapter 7.

References

[Aud07] A. Audren, A. Benyagoub, L. Thome and F. Garrido, Nucl. Instrum. Meth. Phys. B 257 (2007) 227.

[Aud08] A. Audren, A. Benyagoub, L. Thome and F. Garrido, Nucl. Instrum. Meth. Phys. B 266 (2008) 2810.

[Bra88] E. Brady and J. Holum, 'Fundamentals of Chemistry', John Wiley and Sons, Inc, 1988.

[Bor94] N. Borisov, L. Borisova, B. Bylkin, S. Tsvetkov, G. Momot and A. Khulev, At. Energ. 76 (1994) 146

[Chr85] A. Christ, W. Mehner and W. Schenk, IAEA Specialists Meeting on Fission Product Release and Transport in Gas-Cooled Reactors, Berkeley, UK (1985) 30

[Dev00] R. Devanathan and W. Weber, Nucl. Mater. 278 (2000) 258.

[Eld09] R. Elder and R. Allen, Prog. Nucl. Energ. 51 (2009) 500.

[Got90] H. Gottaut and K. Kruger, Nucl. Engrg. Des. 121 (1990) 143.

[Han03] D. Hanson, "A Review of Radionuclide Release from HTGR Cores during Normal Operation", EPRI, Palo Alto, CA (2003) 1009382.

[Lil93] S. Lilov, Mat. Sci. Engrg. B 21 (1993) 65.

[McH93] C. McHargue and J. Williams, Nucl. Instrum. Meth. Phys. B 80 (1993) 889.

[Moo08] R. Moormann, Sci. and Tech. Nucl. Install. (2008). 597491. 2.

[Nic02] H. Nickel, H. Nabielek, G. Pott and A.W. Mehner. Nucl. Engrg. Des. 217 (2002) 14.

[Pir93] P. Pirouz and J.W. Yang, Ultramicroscopy. 51 (1993) 189.

[Sch90] W. Schenk, G. Pott and H. Nabielek, Nucl. Mater. 171 (1990) 19.

[Soh06] R. Sohal, "CVD Growth of (001) and (111) 3C-SiC Epilayers and Their Interface Reactivity with Praseoydmium Oxide Dielectric layers" PhD Thesis, Brandenburgische Technische Universität Cottbus, 2006, p.27

[Sne07] L. Snead, T. Nozawa, Y. Katoh, T. Byun, S. Kondo and D. Petti, Nucl. Mater. 371 (2007) 329.

[Yua02] L. Yuanzhong and C. Jianzhu, Nucl. Engrg. Des. 218 (2002) 81.

[Wan08] J. Wang, "Developing a High Thermal Conductivity Nuclear Fuel with Silicon Carbide Additives" PhD Thesis, University of Florida, 2008, p.22

[Wen98] E. Wendler, A. Heft and W. Wesch, Nucl. Instrum. Meth. Phys. B 141 (1998) 105.

[Wes95] W. Wesch, A. Heft, E. Wendler, T. Bachmann and E. Glaser, Nucl. Instrum. Meth. Phys. B 96 (1995) 335.

[Wes96] W. Wesch, Nucl. Instrum. Meth. Phys. B 116 (1996) 305.

[Wol05] M. Wolborski, "Termination and Passivation of Silicon Carbide Devices", Licentiate Thesis, Royal Institute of Technology (KTH), Department of Microelectronics and Information Technology, 2005, p.5

[www1] http://www.pbmr.co.za. (09-02-2010).

[Zso05] Z. Zolnai, "Irradiation-induced Crystal Defects in Silicon Carbide", PhD Thesis, BUTE-DAP, Department of Atomic Physics, 2005, p.4

Chapter 2: Diffusion

The process by which matter is transported from one part of a medium with a higher concentration to another with a lower concentration as a result of random motion is known as diffusion. Random walk theory is used to characterize the motion of the particles of diffusing substance. In a one dimensional system, each particle has equal probability of moving in a direction either side of its initial position, that is, the particle has no preferred direction of motion for a given time interval. The net flow of matter in the medium is governed by the concentration gradient, with particles moving from a region of higher concentration to a region of lower concentration. The flow down the concentration gradient is not influenced by a bias towards a particular direction, the net flux results from the fact that there are more atoms that randomly move in the region of higher concentration than in the region of lower concentration.

2.1 The Diffusion Coefficient

If we consider a reference plane and the direction x perpendicular to that plane, an expression relating the flux J, to the concentration gradient $\partial C/\partial x$ and the diffusion coefficient D, can be written as:

$$J = -D\frac{\partial C}{\partial x} \tag{2.1}$$

here C is the concentration of the diffusing substance. Equation (2.1) is known as Fick's first law [Cra75, Jos60]. The diffusion coefficient, also known as the diffusivity, gives a measure of the ease with which particles move in a medium, that is how far the particle can move within a given time interval. For an isotropic medium, in three dimensions, Fick's first law can be written as:

$$\bar{J} = -D\nabla C \tag{2.2}$$

Fick's second law, widely regarded as the general diffusion equation, is derived from equation (2.1) and the continuity equation.

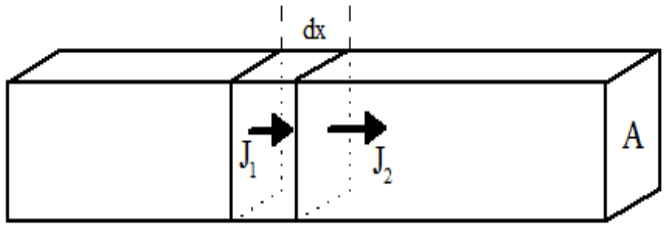

Figure 2.1: A differential volume element in a bar of cross-sectional area A, with impurity flux into and out of the volume J_1 and J_2 respectively. Taken from [Cam96].

For the long bar of material in Fig. 2.1, with cross section A, and considering a small volume of length dx, and a one dimensional flux, J_1 entering the volume ,and flux J_2 leaving the volume [Cam96], we have,

$$\frac{J_2 - J_1}{dx} = \frac{\partial J}{\partial x} \tag{2.3}$$

For the case $J_2 \neq J_1$, the concentration of the diffusing substance in the small volume element of the bar will change. With the number of impurity atoms in the volume element being given by the product of the concentration and the differential volume element ($A \cdot dx$), the continuity equation is then:

$$-A(J_2 - J_1) = -A \cdot dx \frac{\partial J}{\partial x} = A \cdot dx \frac{\partial C}{\partial t} \tag{2.4}$$

Equation (2.4) can thus be presented as

$$\frac{\partial C}{\partial t} = -\frac{\partial J}{\partial x} \tag{2.5}$$

Incorporating Fick's first law, equation (2.1) into equation (2.5) yields the general form of Fick's second law.

$$\frac{\partial C}{\partial t} = \frac{\partial}{\partial x}\left(D\frac{\partial C}{\partial x} \right) \tag{2.6}$$

Based on the assumption that the diffusion coefficient is independent of position, Fick's second law reduces to

$$\frac{\partial C}{\partial t} = D\frac{\partial^2 C}{\partial^2 x} \tag{2.7}$$

For an isotropic medium, in three dimensions, Fick's second law is expressed as:

$$\frac{\partial C}{\partial t} = D\nabla^2 C \tag{2.8}$$

The temperature dependence of the diffusion coefficient [Sha73] is given by an Arrhenius equation:

$$D = D_0 \exp\left(\frac{-E_A}{kT} \right) \tag{2.9}$$

E_A is the activation energy, k is the Boltzmann constant, D_0 is a temperature independent pre-exponential factor and T the temperature in units of Kelvin.

2.2 Evaluation of the Diffusion coefficient

Several methods of obtaining the general solutions of the diffusion equation (2.7) for a variety of initial and boundary conditions are discussed in the book "*The Mathematics of Diffusion*" by Crank [Cra75]. In this work, in order to describe the spreading by diffusion of the implanted iodine with annealing time, we have used the solution shown in equation (2.10) [Mye73]. This method assumes that the original implanted profile is purely Gaussian and gives the diffused profile as

$$C(x,t) = \left[2(\pi Dt)^{1/2}\right]^{-1} \int_0^\infty C_0(y) \times \left(e^{-(y-x)^2/4Dt} + e^{-(y+x)^2/4Dt}\right) dy \qquad (2.10)$$

To obtain this solution the initial condition

$$\lim_{x \to 0}\left(\frac{\partial}{\partial x} C(x,t)\right) = 0$$

is used, with $C_0(x) = C(x,0)$ representing the initial iodine profile.

The initial profile $C_0(x)$ is taken to be:

$$C_0(x) = K(\pi D t_0)^{-1/2} e^{-x^2/4Dt_0} \qquad (2.11)$$

where K is an adjustable constant. The concentration profile in equation (2.10) reduces to a Gaussian function of the form:

$$C(x,t) = K[\pi D(t + t_0)]^{-1/2} e^{-x^2/4D(t+t_0)} \qquad (2.12)$$

In the dilute limit, the concentration profile will remain a normal distribution with annealing time t in an infinite medium and equation (2.12) can generally be expressed as:

$$C(x,t) = K[\pi Dt]^{-1/2} \exp\left(-x^2/4Dt\right) \tag{2.12}$$

Defining the profile width $W(t)$ as the full width at half maximum (FWHM), the relationship between the final and initial widths will given by

$$[W(t)]^2 = 4Dt\ln(2) + [W(0)]^2 \tag{2.13}$$

Therefore from the change in the FWHM of a Gaussian depth distribution, the slope of a plot of $[W(t)]^2$ versus the annealing time t at constant temperature will yield the diffusion coefficient D.

2.3 Mechanisms of Diffusion in Solids

Diffusion does not take place in an ideal crystal. An enormous amount of energy would be required to break the bonds between lattice atoms and cause atoms to jump simultaneously and exchange positions. In real crystals, the mobility of atoms is enhanced by the presence of defect structures like point defects such as vacancies and interstitials (Frenkel-pairs) as well as extended defects like point defect clusters, dislocations and grain boundaries. The atoms oscillate in their equilibrium positions with frequencies of the order of the Debye frequency which is approximately 10^{12} Hz [Hei05] until they acquire enough energy to surpass the potential barrier jump from one site to another, leading to diffusion in the solid. In semiconductors, there are two major mechanisms of diffusion, the vacancy mechanism and the interstitial mechanism.

2.3.1 Vacancy Mechanism

Unoccupied lattice sites, known as vacancies, provide the favourable route for atomic diffusion. In the vacancy mechanism [She89], atoms from adjacent sites can jump into a nearby vacancy. The atoms sitting next to a vacancy are bonded to fewer atoms as a result of the displacement of one of the lattice atoms, hence less energy is required to

move the adjacent atom into the vacancy than in a direct position exchange between two adjacent atoms without a vacancy between them.

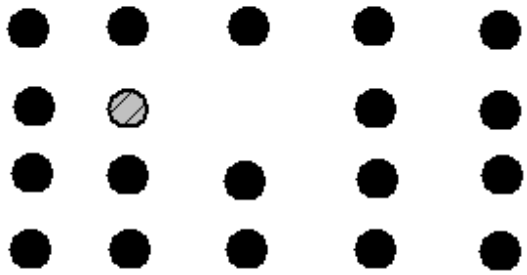

(a)

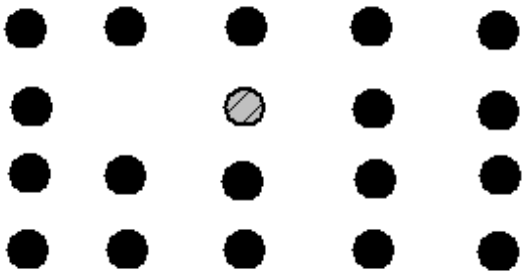

(b)

Figure 2.2 (a) and (b) show the diffusion of an impurity by vacancy exchange.

2.3.2 Interstitial Mechanism

An atom diffusing interstitially [She89] meanders from one interstitial site to another without displacing any of the lattice atoms. These solute atoms are usually smaller than

lattice atoms and can easily move from one interstitial site to the next. This mechanism is commonly referred to as the direct interstitial mechanism. Another form of the interstitial mechanism is the interstitialcy mechanism where self interstitials push one of their neighbours into an interstitial position and occupy the lattice site previously occupied by the atom it has displaced.

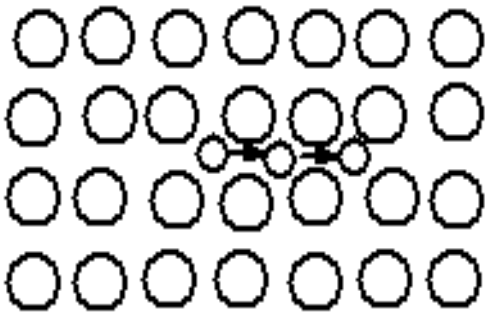

Figure 2.3: Diffusion of an impurity atom via the interstitial mechanism.

References

[Cam96] S. Campbell, "The Science and Engineering of Microelectronic Fabrication", Oxford University Press, 1996, p.40

[Cra75] J. Crank, "The Mathematics of Diffusion", Oxford University Press, Bristol, 1975, p.2

[Hei05] P. Heitjans and J. Karger, "Diffusion in Condensed Matter", Springer, Netherlands, 2005, p.22

[Jos60] W. Jost, "Diffusion in Solids, Liquids and Gases", Academic Press, New York, 1960, p.2

[Mye73] S. Myers, S. Picraux and T. Prevender, Phy. Rev B. 9/ 10 (1973) 3953.

[Sha73] D. Shaw, "Atomic Diffusion in Semiconductors", Plenum Press, London, 1973, p.3

[She89] P. Shewmon, "Diffusion in Solids", The Minerals, Metals and Materials Society, U.S.A, 1989, p.57

Chapter 3: Ion implantation

3.1 Introduction

Ion implantation is regarded as the main technique used to introduce controlled concentrations of impurities into solids. Atoms from the desired material are ionized, then accelerated and directed towards a target. The kinetic energy of the ions enables them to penetrate into the lattice of the target material. Energetic particles impinging on a target, penetrating into it until they come to rest somewhere within the target are said to have been implanted. During ion-solid interactions, ions gradually lose energy when they interact with target atoms as they move through the solid until they stop at a certain depth within the solid.

3.2 Energy loss of ions in solids

There are two major processes which results in the ions losing energy that occur when energetic ions enter a solid. The ions lose energy when they undergo elastic collisions with lattice atoms and the ions also lose energy in inelastic interactions with electrons in the solid in which the electrons are excited. These processes are referred to as nuclear energy loss and electronic energy loss respectively. The two processes are generally viewed as being independent from each other [Wil73].

In nuclear stopping, elastic coulomb interactions between the nuclei of the ion and target atom resulting in relatively large amounts of energy and momentum transfer, lead to significant changes in ion's direction as well as displacements of target atoms from their lattice positions. Nuclear stopping depends on the distance of closest approach of the ion to the target atom as the interaction potentials are strongly dependant on the distance separating the two nuclei. In the case of electronic stopping, the collisions are characterized by relatively small amounts of energy and momentum transfer due to the small electron mass. For such collisions, deflections will be negligible.

3.3 Energy dependence of nuclear and electronic stopping

Nuclear energy loss is the dominant process in stopping the ion at low energies while at the higher energies, electronic stopping is the major factor in the stopping process. At the energies that are considered to be low [Tes95, Hay95], the velocity v of the ion, will be far less than a critical velocity v_1 of the valence electrons of the ion and the ion retains its electrons and is neutralised by electron capture. Elastic collisions with the target nuclei dominate at these velocities, thus nuclear stopping is more pronounced. v_1 is given by

$$v_1 = v_0 Z_2^{2/3} \tag{3.1}$$

The Bohr velocity v_0 given by

$$v_0 = e^2/h \tag{3.2}$$

Z_2 represents the atomic number of the target atom, e is the electronic charge and h is the Planck constant.

As the ion velocity is increased nuclear stopping becomes less pronounced and electronic stopping becomes the dominant process. Nuclear, stopping reaching a maximum value in the region where, v, the ion velocity is approximately equal to the velocity in equation (3.1). At a velocity $v \leq v_0 Z_2^{2/3}$ only electrons near the Fermi level are excited and involved in the electronic energy loss process. For higher velocities, $v >> v_0 Z_2^{2/3}$, the ion is stripped of all its electrons and the electronic energy loss is mainly due to ionization of target atoms.

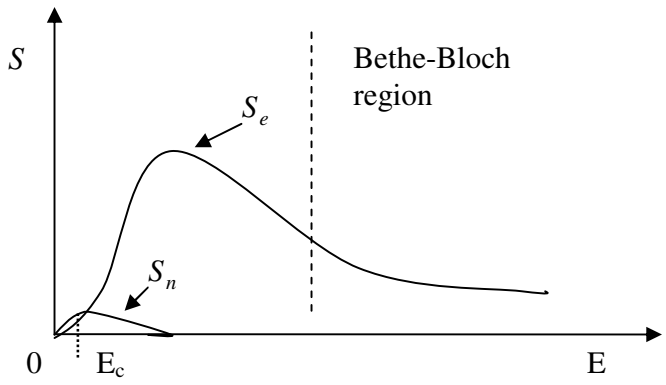

Figure 3.1: The nuclear S_n and electronic S_e cross sections as a function of the incident particle energy E. E_c is the critical energy where the contributions of nuclear and electronic cross sections are the same.

3.3.1 Stopping power

The rate at which the ion loses energy, E , with distance traveled , x , dE/dx is known as the specific energy loss or the stopping power. The total stopping power [Dear73] is considered to be the sum of the two independent processes involved in the stopping, which are the electronic and nuclear stopping and can be written as

$$-\frac{dE}{dx} = N\left[S_n(E) + S_e(E)\right] \tag{3.3}$$

Where N is the atomic density of the target, $S_n(E)$ and $S_e(E)$ are the nuclear and electronic stopping cross sections respectively.

The stopping cross-sections are defined by:

$$S_n = \left(\frac{1}{N}\right)\left(\frac{dE}{dx}\right)_n \quad \text{and similarly} \quad S_e = \left(\frac{1}{N}\right)\left(\frac{dE}{dx}\right)_e \tag{3.4}$$

The respective nuclear and electronic energy loss relations [Fel86]:

$-\left.\frac{dE}{dx}\right|_n$ and $-\left.\frac{dE}{dx}\right|_e$, are given in equations (3.5) and (3.6) below

$$-\left.\frac{dE}{dx}\right|_n = \frac{4\pi Z_2^2 Z_1^2 e^4 N}{M_2 v^2} \ln\frac{2mv^2}{I} \tag{3.5}$$

$$-\left.\frac{dE}{dx}\right|_e = \frac{4\pi Z_1^2 e^4 N Z_2}{m_e v^2} \ln\frac{2mv^2}{I} \tag{3.6}$$

In the above relations, I is a displacement energy and in equation (3.6), the energy I, represents an average over the various excitations of the electrons in the target. This average excitation energy, I is generally considered to be roughly $10Z_2$ in eV. N is the atomic density of the stopping medium, Z_2 is the atomic number of the stopping atoms, Z_1 is the atomic number of projectile ion, e, the electronic charge, m_e is the electron mass and M_2 is the mass of the target particles.

In targets in which more than one element is present, collisions are still viewed as independent encounters taking place one at a time. The collisions will be distributed among the various elements and weighted proportionally to the elemental distribution in the compound. This is known as Bragg's rule. The stopping cross section $S^{A_mB_n}$ of a target with composition A_mB_n is then

$$S^{A_mB_n} = mS^A + nS^B \tag{3.7}$$

S^A and S^B are the stopping cross sections of target atoms A and B.

Having established the rate of energy loss with distance, the total distance that the ion will travel in slowing down and coming to rest in the solid commonly referred to as the range, can be found by integrating the specific energy loss over the interval $0 \le E \le E_0$, where $E_{0,}$ is the energy of the incident ion beam.

$$R_{tot} = \int_0^E \frac{dE}{-(dE/dx)} \tag{3.8}$$

An energetic ion will be involved in a series of many individual collisions with target atoms at various impact parameters resulting in different scattering angles. Ions in an ion beam initially having the same energy will be scattered in many different directions through different angles and will therefore not follow the same path but will travel in many different directions. A useful quantity used in range theory is then a projection of the distance traveled by the ion through the solid in a direction perpendicular to the surface. This quantity is called the projected range R_P. The projected range gives a measure of the approximate depth within the solid the ion reaches before it is stopped. The statistical nature of the collision processes will result in the impurity concentration $N(x)$ having a depth distribution which is approximately Gaussian [Cam96]

$$N(x) = \frac{\phi}{\sqrt{2\pi}\Delta R_P} e^{-(x-R_P)^2/2\Delta R_P^2} \tag{3.9}$$

R_P the mean projected range, ΔR_P is the standard deviation of the projected range and ϕ is the implanted fluence.

There are many distribution functions to represent the actual impurity concentration $N(x)$. In this study we have used the function shown below in equation (3.10) to describe the concentration $C(x,t)$ as stated in section 2.2 of chapter 2.

$$C(x,t) = K[\pi Dt]^{-1/2} \exp(-x^2/4Dt) \tag{3.10}$$

3.4 Implantation Damage

Chemical bonds between lattice atoms are generally of the order of a few eV. At energies associated with ion implantation, the energy transferred to the lattice atoms is more than enough to break the bonds and displace atoms from their lattice sites. The amount of energy transferred when such an elastic collision occurs depends on the atomic numbers, the atomic masses of the particles involved and their impact parameter. Maximum energy transfer takes place when the magnitude of the impact parameter is zero, which is during a head on collision, and the maximum energy transferred, T_m is given by [Frie01]

$$T_m = \frac{4M_1M_2}{(M_1+M_2)^2}E \tag{3.11}$$

Where M_1, and M_2 are the masses of the ion, target atom respectively and E is kinetic energy of the projectile ion. However most collisions are not head on and less energy is transferred during the collision and the energy transferred is expressed by

$$T = T_m \cos^2\psi \tag{3.12}$$

where ψ is the angle of recoil of the target atom.

A threshold value of the energy exists such that above this energy, an atom that has been displaced from its lattice site will move to a region well outside the spontaneous recombination zone, leaving a vacancy at the lattice site. This energy is called the displacement energy. The high energies employed in ion implantation result in large energy and momentum transfers to the extent that the displaced atoms themselves recoil with energies to displace further lattice atoms, leading to a collision cascade. This primary knock on atom, generally produces many displacements before dissipating all of its energy. The entire collision sequence is quenched in about 10^{-11} s [Wil98]. Depending on implantation temperature, implanted species and the target material itself, the density of defects created can be high and very stable in the solid. Higher implantation fluence can cause the various collision cascades to overlap until threshold fluence results in a previously crystalline substrate losing any long range order, a condition referred to as amorphous. If no annealing of damage occurs during implantation [Wil98], amorphization should occur at a fluence where each atom has been displaced at least once, that is at 1dpa (dpa standing for displacement per atom). A higher substrate temperature will result in annealing of some of the damage formed during implantation and a larger fluence will be required for amorphization to occur.

References

[Cam96] S. Campbell, "The Science and Engineering of Microelectronic Fabrication", Oxford University Press, 1996, p.106

[Dea73] G. Dearnaley, J. Freeman, R. Nelson and J. Stephen, "Ion implantation" , North-Holland Publishing Company, Netherlands, 1973, p.10

[Fri01] E. Friedland, "Radiation Damage in Metals", Crit. Rev. Sol. Stat. Mater. Sci. 25 (2001) 88.

[Hay95] M. Hayes, "Determination of implantation by (p, γ) - resonance reactions" PhD Thesis, Department of Physics, University of Pretoria, 1995, p.4

[Tes95] J. Tesmer and M. Nastasi, "Handbook of modern ion beam materials analysis", Materials Research Society, Pittsburg, 1995

[Wil73] R. Wilson and G. Brewer, "Ion beams, with applications to ion implantation", John Wiley and Sons Inc., New York, 1973, p.268

[Wil98] J. Williams, Mat. Sci. Eng. A 253 (1993) 1.

Chapter 4: Rutherford Backscattering Spectroscopy (RBS)

Rutherford backscattering spectroscopy has evolved into one of the most valuable analytical techniques in materials analysis giving quantitative information on chemical composition, depth distribution and crystal quality. RBS allows for quick and non destructive analysis of materials. In essence, it is a very simple experiment based on the principle that, when light ions e.g. He and H in the MeV range are incident on a target material, the majority of the ions come to rest in the solid while a small percentage of the ions are scattered back at angles larger than 90° relative to the direction of incidence. These backscattered particles can then be detected at a set angle. These interactions involving large angle scattering result from close impact collisions governed by Coulomb repulsion between positively charged nuclei.

4.1 Rutherford differential cross section

The yield or the total number of the backscattered and detected particles from a volume element of atoms representing one channel in a thick target [Feld86] is given by

$$Y = \sigma \cdot \Omega \cdot Q \cdot N_s \qquad (4.1)$$

where Ω is the detector solid angle, Q, the total number of incident particles and is determined by the time integration of the current of charged particles incident on the target. $N_s = Ndx$ is the number of target atoms /cm^2, analysed by that channel and N is the volume density of atoms in the target and dx is the channel width. σ here is the scattering cross section.

The differential cross section is a measure of how frequently a collision in a scattering event at a particular solid angle actually occurs. It connects the backscattering yield to quantitative analysis. In backscattering spectroscopy [Gro84], at the energies of interest

to our work, the distance of closest approach between the projectile ion and target atom is considered to be large compared to nuclear dimensions. However, this distance is taken to be small compared to the Bohr radius (0.53 Å). Under these conditions, the interaction can be viewed as an unscreened Coulomb repulsion between two positively charged nuclei. The Rutherford differential cross section [Fel86, Chu78] shown in equation 4.2 can then be used. Here the differential cross section is given in the laboratory coordinate system by:

$$\frac{d\sigma}{d\Omega} = \left(\frac{Z_1 Z_2 e^2}{4E}\right)^2 \left[\sin^{-4}\frac{\theta}{2} - 2\left(\frac{M_1}{M_2}\right)^2 + \cdots\right] \tag{4.2}$$

Z_1 is the atomic number of the projectile ion of mass M_1, Z_2 is the atomic number of target atom having a mass M_2, e is the electronic charge, E the energy of the ion immediately before scattering and θ is the scattering angle.

From equation (4.2), the Rutherford backscattering probability of a particle [Fel86, Chu78], is mainly influenced by the following factors:

- The atomic number of the projectile ion Z_1. $d\sigma/d\Omega \propto Z_1^2$, the yield increases with atomic number.
- The atomic number of the target atom Z_2. $d\sigma/d\Omega \propto Z_2^2$, RBS is much more sensitive to heavy elements than to light ones
- The differential cross-section is inversely proportional to the square of the energy, $d\sigma/d\Omega \propto E^{-2}$. The backscattering yield decreases sharply with increasing energy.

4.2 The Kinematic Factor

The energy of a backscattered particle depends on its own mass, M_1, the mass of the target M_2 and the backscattering angle θ as measured in the laboratory reference system. The ratio of the projectile energy after collision E_1 to that before collision E_0 [Chu78] is known as the kinematic factor (4.3).

$$K = \frac{E_1}{E_0} = \left[\frac{\left(M_2^2 - M_1^2 \sin^2 \theta\right)^{\frac{1}{2}} + M_1 \cos\theta}{M_2 + M_1} \right]^2 \tag{4.3}$$

The kinematic factor is only dependent on the masses and on the scattering angle. Knowing the energy of the incident beam and the mass of the projectile, by simply measuring the energy of the backscattered ions, the mass of the target atom involved in the collision can be calculated. The kinematic factor leads to mass analysis in RBS.

4.3 Depth Profiling

The ability to resolve the energy differences between particles backscattered at different depths within the target material is one of the key features of RBS. For the case of the scattering of a projectile by atoms below the surface of a target material, the energy E immediately before scattering is less than the initial projectile energy E_0 as the ion loses energy on the inward path when penetrating the target. After scattering, the particle also loses energy on its outward path, emerging from the sample with energy E_1. This energy E_1 of the detected particles can be related to the depth at which the particle scattering event occurred and the backscattering yield with a particular energy in turn depends on the number of atoms present at that depth.

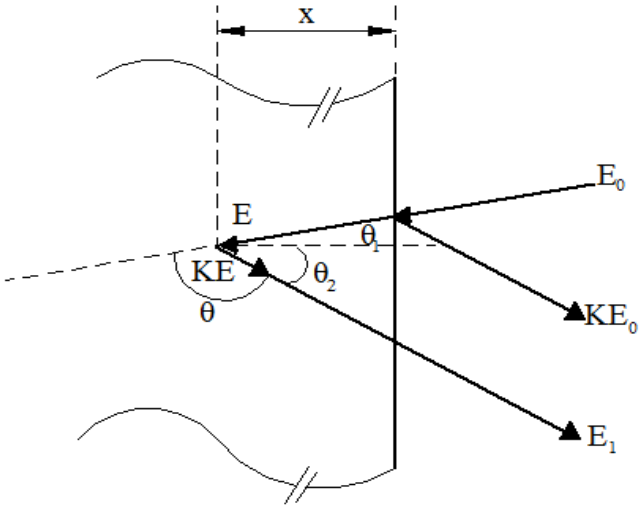

Figure 4.1: Energy loss components of a projectile scattered from depth x. Taken from [Chu78]

A schematic of the geometry of the scattering of a particle of initial energy E_0 at a depth x is shown in Fig. 4.1. The energy E immediately before scattering can be related to the incident path length $x/\cos\theta_1$ by

$$x/\cos\theta_1 \propto -\int_{E_0}^{E} dE/(dE/dx) \tag{4.4}$$

and the outward path length $x/\cos\theta_2$, related to KE and E_0 by

$$x/\cos\theta_2 \propto -\int_{KE}^{E_1} dE/(dE/dx) \tag{4.5}$$

The energy KE_0 is the energy corresponding to the energy of particles backscattered from atoms on the surface of the target. $E_0 - E$ is the energy loss along the inward path,

ΔE_{in} and $KE - E_1$, the energy loss along the outward path, ΔE_{out}. When an assumption is made that the rate of energy loss with distance, dE/dx is constant along the inward and outward paths (surface energy approximation) [Chu78], equations (3.4) and (3.5) reduce to

$$E = E_0 - \frac{x}{\cos\theta_1}\left.\frac{dE}{dx}\right|_{in} \tag{4.6}$$

and

$$E_1 = KE - \frac{x}{\cos\theta_2}\left.\frac{dE}{dx}\right|_{out} \tag{4.7}$$

the subscripts, in and out, referring to the constant values of dE/dx along the inward and outward paths.

Since E_1 is the measured value of the energy of a particle scattered from an atom at depth x, from equations (4.6) and (4.7), the energy difference ΔE between E_1 and KE_0 is thus given by

$$\Delta E = KE_0 - E_1 = [S]x \tag{4.8}$$

With $[S]$ being the energy loss backscattering factor [Chu78]

$$[S] = \frac{K}{\cos\theta_1}\left.\frac{dE}{dx}\right|_{in} + \frac{1}{\cos\theta_2}\left.\frac{dE}{dx}\right|_{out} \tag{4.9}$$

The backscattering energy loss factor allows for a depth scale to be applied to a backscattering energy spectrum. A measured energy spectrum can therefore directly be converted into a depth scale. In practice, the energy to depth conversion is performed numerically using tabulated values of the stopping powers [Zie77]. In this work we have used the computer code A-Stop2 [Fri09].

In a compound target, as is the case with our material of interest, SiC, the energy loss is calculated from the stopping power of the projectile in the compound. Bragg's rule [Chu78] on the additivity of stopping cross sections of the elements making up the target is used. Defining the compound as A_mB_n, the energy loss of a particle backscattered from element A at a depth x can be stated in the form given by equations (4.8) and (4.9) as

$$\Delta E_A = [S]_A^{A_mB_n} x = \left(\frac{K_A}{\cos\theta_1} \frac{dE}{dx}\bigg|_{in} + \frac{1}{\cos\theta_2} \frac{dE}{dx}\bigg|_{out} \right) x \tag{4.10}$$

Similarly for element B in the compound,

$$\Delta E_B = [S]_B^{A_mB_n} x = \left(\frac{K_B}{\cos\theta_1} \frac{dE}{dx}\bigg|_{in} + \frac{1}{\cos\theta_2} \frac{dE}{dx}\bigg|_{out} \right) x \tag{4.11}$$

In the expressions above, K_A and K_B are the kinematic factors of elements A and B in the compound. $[S]_A^{A_mB_n}$ and $[S]_B^{A_mB_n}$ are stopping cross sections of the elements making up the compound.

From Bragg's rule, as stated in section (3.3.1) the total stopping cross section $S^{A_mB_n}$ of a target A_mB_n is then

$$S^{A_mB_n} = mS^A + nS^B \tag{4.12}$$

S^A and S^B are the stopping cross sections of target atoms A and B.

The total energy loss in the compound can then be given as:

$$\Delta E = [S]^{A_mB_n} x = \frac{m}{m+n}[S]_A^{A_mB_n} x + \frac{n}{m+n}[S]_B^{A_mB_n} x \tag{4.13}$$

4.4 Height of backscattering spectrum

The height of a backscattering spectrum H gives the number of backscattered particles with energy in a certain energy interval (energy width of a channel) E to $E+\delta E$. The energy width is determined by the electronic setting of the detecting system. This height is given by [Chu78]:

$$H = Q\Omega\left(\frac{d\sigma}{d\Omega}\right)N\frac{\delta E}{[S]\cos\theta_1} \tag{4.14}$$

In equation (4.14) Q is the total number of incident particles, Ω is the detector solid angle, N is the atomic density of the target, while $\left(d\sigma/d\Omega\right)$ and $[S]$ are given by equations (4.2) and (4.9) respectively.

For a compound target as is the case with SiC, the height of the spectrum peak for element A, in the compound A_mB_n, H_A can be written as:

$$H_A = Q\Omega\left(\frac{d\sigma}{d\Omega}\right)_A N_A \frac{\delta E}{[S]_A^{A_mB_n}\cos\theta_1} \tag{4.15}$$

And similarly for element B in the compound:

$$H_B = Q\Omega\left(\frac{d\sigma}{d\Omega}\right)_B N_B \frac{\delta E}{[S]_B^{A_mB_n}\cos\theta_1} \tag{4.16}$$

The energy spectrum of such a compound is then a superposition of the two signals from the elements A and B. The edge of each signal of the elements is defined by the kinematic factor of each element in the compound. Taking $H_A(E_1)$ and $H_B(E_1)$ as the heights of the individual signals generated by particles detected with energy E_1, after scattering from A and B, the total height of the spectrum [Chu78] is given by

$$H(E_1) = H_A(E_1) + H_B(E_1) \tag{4.17}$$

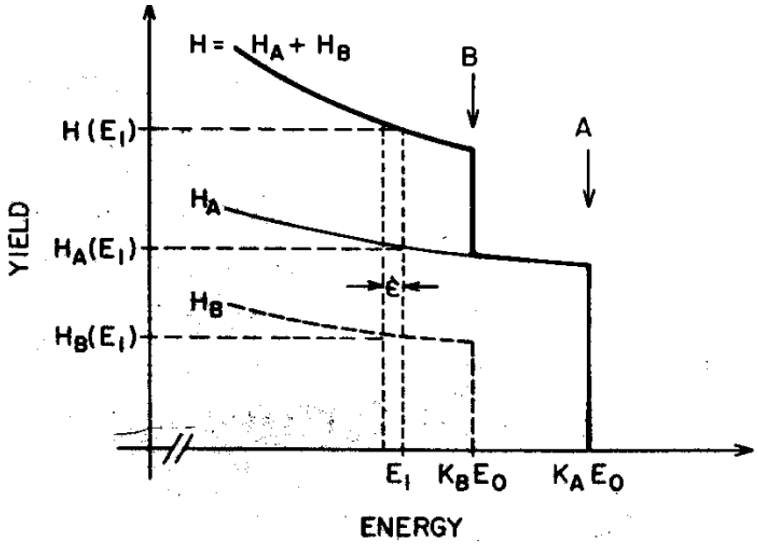

Figure 4.2: Backscattering spectrum of a homogeneous mixture of two elements *A* and *B*. Taken from [Chu79].

The edge of the signal is defined by the kinematic factor K of the two elements with heavy masses going to the high energy side and low masses appearing on the low energy side of the spectrum.

4.5 Energy Straggling

A phenomenon referred to as energy straggling places a limit to which energy losses and therefore depths can be resolved in backscattering spectrometry. The discrete nature of the energy loss process leads to a wide range of impact parameters and atomic excitation parameters. Identical particles initially having the same velocity will not necessarily have the same energy after traversing the same thickness in a homogenous target. The resulting statistical uncertainty in the energy of particles penetrating a solid, leads to a statistical distribution in both the number and size of events for a certain depth of penetration. As a result the energy profile broadens as a function of the distance traveled through the target. This energy loss along a given path length is distributed around a mean value. According to Bird *et al,* [Bir89] the variance, Ω^2, in the number of collisions experienced by an energetic particle when passing through a solid of thickness t, having atomic density N is given by

$$\Omega^2 = 4\pi\left(Z_1 e^2\right)^2 N Z_2 t \qquad (4.18)$$

Z_1 and Z_2 are the atomic numbers of the ion and target respectively. The energy distribution at a given depth is assumed to be Gaussian. The FWHM for energy straggling is 2.35Ω.

4.6 Channeling

When energetic ions are incident along the open low index crystallographic directions (channels) in a crystalline target, they can experience an enhanced penetration. The ions are steered along the open crystal direction by a series of correlated collisions with the regular array of lattice atoms and are said to have been channeled. The open channels in a crystal have two forms. One form is the axial channel, where the channels are defined by rows of atoms. The other form is the so called planar channel where the open direction is defined by parallel atomic planes [Bir89]. For this channeling to occur, the angle of incidence of the ions must be smaller than a critical angle, ψ_0 such that the ions are reflected away from the row of atoms continuously by the correlated series of many consecutive glancing collisions with the atoms in the row. The critical angle is given by [Gem74]:

$$\psi_0 = \left(2Z_1 Z_2 e^2 / Ed\right)^{1/2} \tag{4.19}$$

E is the incident ion energy, d is the inter atomic spacing along the axial direction, Z_1 and Z_2 are the atomic numbers of the ion and target respectively. Above this critical angle [Gem74], the particles begin to approach the row of atoms so closely that the particle will start to feel effect the atoms in the row individually and the particle will experience large angle scattering and will be dechanneled. When these incidence conditions for channeling to occur are fulfilled, meaning that projectiles only suffer smooth collisions with very little deviation from their original direction, the energy loss per unit length is reduced and their range is increased [Gro84]. The cross section of events that require close collisions with atoms is greatly reduced during channeling. Examples of such events include X-ray production, nuclear reactions and Rutherford backscattering.

The so called continuum potential can be used to describe the axial channeling [Gem74]. This potential is given by [Bir89]:

$$U(r)=\frac{1}{d}\int_{-\infty}^{\infty}V\left[\left(z^2+r^2\right)^{1/2}\right]dz \tag{4.20}$$

here V is the interatomic potential and d, r and z are defined in Fig. 4.3 as shown below

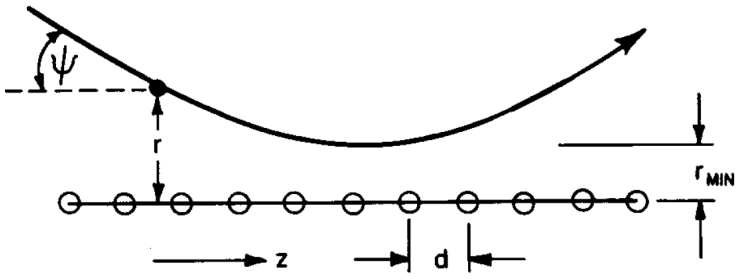

Figure 4.3: Ion scattering from an axial string of atoms. Taken from [Bir89].

In the continuum potential, the scattering is approximated from of a string of atoms. The discrete nature of the atoms in the string is assumed to be negligible and each steering collision is taken as an average of many individual ion-atom collisions [Bir89]

The alignment of an ion beam with a low index direction (axial alignment) [Bir89] can result in approximately 95% of the incident ions being channeled resulting in a corresponding decrease of the yield of backscattered ions from small impact parameter interaction processes. Planar alignment results in a higher backscattering yield of about 30% of the normal (random yield). Fig. 4.4 shows the normalized yield of backscattered particles for planar and axial channeling.

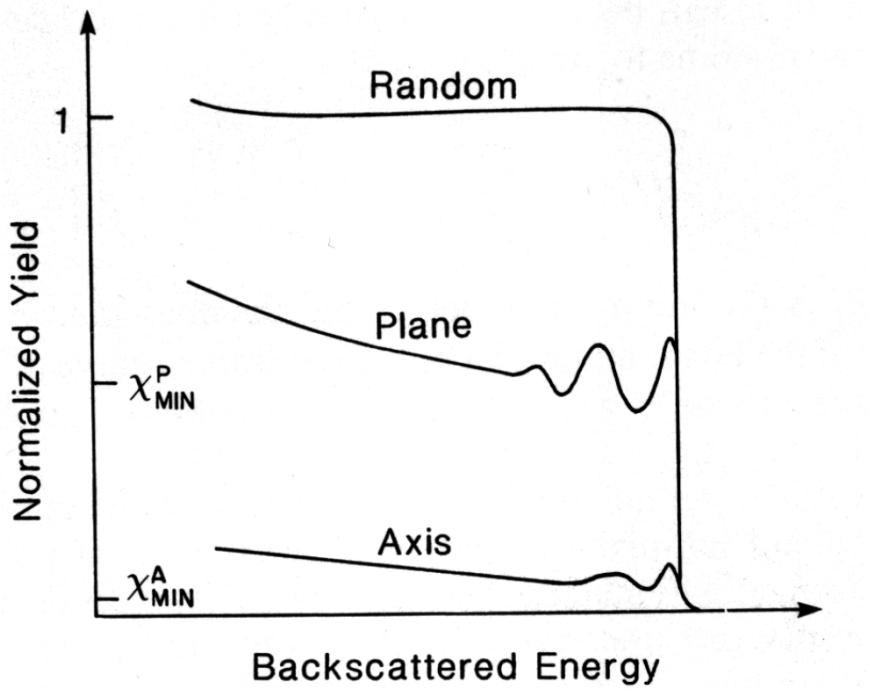

Figure 4.4: RBS/Channeling spectra of axial and planar channeling. Taken from [Bir89].

Experimentally, crystal alignment [Gro84], is performed by placing the sample at the centre of high precision goniometer. Such a goniometer allows one to tilt and rotate the sample about two or three axes. The stepping motors of the goniometer can make movements with an accuracy of about 0.01° [Gro84]. The incident beam will be aligned with successive lower index planar directions when moving the goniometer. A stereographic projection of the crystal can then be constructed from the positions of the planar minima obtained during the angular scan. The angular yield about axial and planar channels is shown in Fig. 4.5. In Fig. 4.5, $\chi_{\min}$ is the minimum yield which corresponds to the minimum random component of the beam as it enters the crystal and $\psi_{1/2}$ is the angular half width at half height of an angular scan [Bir89].

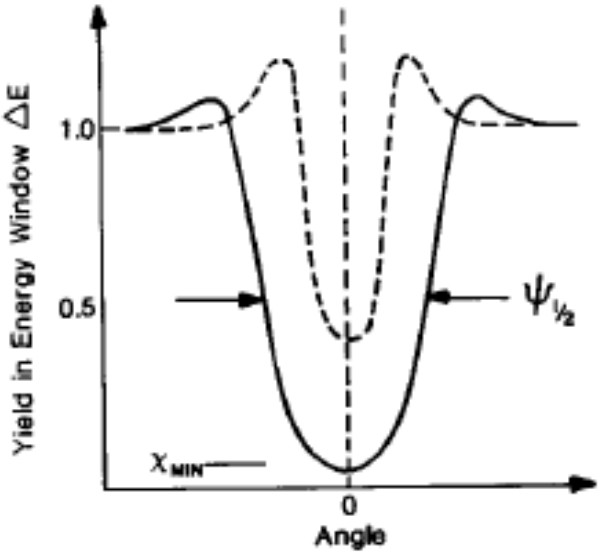

Figure 4.5: The angular yield about an axial channel (solid curve) and a planar channel (broken line). Taken from [Bir89].

The channeling process is very sensitive to small departures from the crystalline structure of a medium. Crystal defects such as displaced lattice atoms, substitutional impurities and interstitial atoms blocking channels can cause dechannelling to occur (Fig. 4.6). In this case there will be a corresponding increase in the yield of backscattered particles.

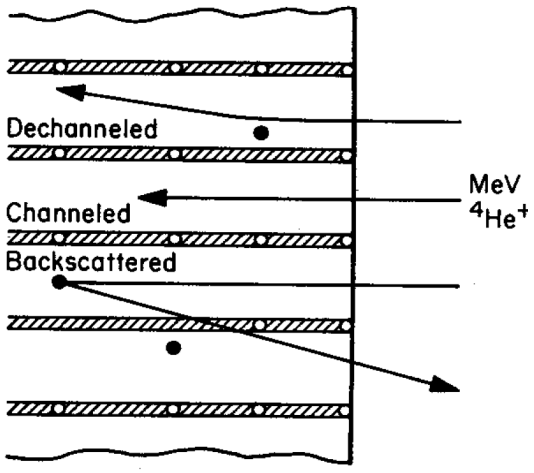

Figure 4.6: Schematic showing the dechannelling and direct backscattering of ions by interstitial atoms blocking a low index direction (channel). Taken from [Chu7].

Channeling techniques combined with the randomly aligned beam in conventional RBS provide information on the amount and depth distribution of lattice disorder in the near surface region of materials and on the thickness of amorphous layers. The extent of disorder in a crystal arising from irradiation can be deduced from RBS combined with channeling techniques. The backscattered yield about an axial channel from a perfect crystal or an un-implanted sample (virgin sample), is very low as compared to the yield about a random direction (Fig. 4.4). Radiation damage production in crystals during ion implantation can be determined by comparing the aligned yield after irradiation with the yield in a random direction. The aligned backscattering yield in general, increases from the levels of the virgin crystal with increasing defect concentration. The production of defects depends on the irradiation conditions like the fluence and irradiation temperature. In RBS [Wes95], the absence of long range order or amorphisation is defined by a relative defect concentration which is equal to unity, which means that the aligned yield reaches the random level. In some cases during ion implantation, the need arises to limit the probability of the channeling of ions incident on a target material. This is usually done by ensuring that the angle of incidence is approximately 7° off axis or by pre-amorphising the near surface region of the crystalline solid.

References

[Bir89] J. Bird and J. Williams, "Ion Beams for Materials Analysis", Academic Press, Australia, 1989, p.620

[Chu78] W. Chu, J. Meyer and M. Nicolet, "Backscattering Spectrometry", Academic Press, New York, 1978.

[Fel86] L. Feldman and J. Meyer, "Fundamentals of Surface and Thin Film Analysis", Elsevier Science Publishing Co, New York, 1986, p.20

[Fri09] E. Friedland, "A-Stop2", Department of Physics, University of Pretoria, 2009. Private communication

[Gem74] D. Gemmell, Rev. Mod. Phys. 46 (1974) 136

[Gro84] J. Grob and P. Siffert, Cryst. Growth. 8 (1984) 59.

[Wes95] W. Wesch, A. Heft, E. Wendler, T. Bachmann and E. Glaser, Nucl. Instrum. and Meth. Phys B 96 (1995) 335.

[Zie77] J. Ziegler, "Helium Stopping Powers and Ranges in All Elements", Pergamon Press, New York, 1977.

Chapter 5: Experimental Techniques

5.1 Iodine implantation

6H-SiC wafers of thickness 0.3 mm and diameter 50 mm produced by Cree Inc®, were implanted with $^{127}I^{+}$ iodine ions by the 400 keV ion implanter Romeo at the Institut für Festkörperphysik Friedrich-Schiller-Universität Jena, Jena, Germany. The 6H-SiC wafers had initially been cleaned by a sequence of ultrasonic agitation in acetone, then deionised water and then methanol to degrease and remove physical contaminants from the surface of the wafers.

The implantations were performed at room temperature at implantation energy of approximately 360 keV up to a fluence of 1 x 10^{16} cm^{-2}. The flux was maintained at a rate below 10^{13} $cm^{-2}s^{-1}$ to minimise the increase in the substrate temperature, thereby reducing the probability of simultaneously annealing some of the radiation damage produced during the room temperature implantations. To avoid channelling effects during implantation, an angle of incidence of the ions was set at an angle of 7° relative to normal incidence.

5.2 Sample Preparation

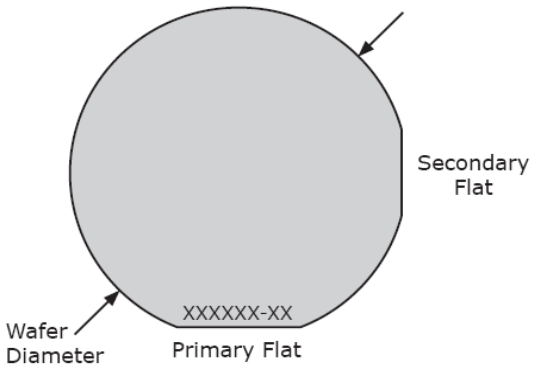

Figure 5.1 6H-SiC wafer procured from Cree Inc® showing the diameter and primary flat along the $[11\bar{2}0]$ direction. Taken from [www2]

The SiC wafer shown in Fig. 5.1 was glued to a brass disc to support the wafer during subsequent cutting processes. The adhesive used was Crystalbond 509™, and the adhesive was heated and smeared over the brass disc. The wafer was then placed on the brass disc and the glue was allowed to cool down establishing firm contact between the brass disc and the wafer. A glass slide was also glued to the other surface to protect that surface. A Struers Accutom variable speed precision cut-off machine was employed to cut the wafer into strips of width approximately 5.5 mm in a direction parallel to the primary flat. A slow cutting rate was used to minimise damage to the wafer surface. Water was applied continuously to the diamond saw blade tip, as a lubricant to wash away the debris during the cutting processes. The strips were then cut in the perpendicular direction at intervals of approximately 5 mm, producing rectangular samples of dimensions of approximately 5.5 mm x 5 mm. The resulting rectangular samples' dimensions ensure that the samples fit well onto the sample holder for analysis in the RBS target chamber. The dimensions of the samples also offer enough area for analysing beam which is collimated to a beam spot of approximately 2 mm^2.

The glue was dissolved by boiling the samples repeatedly in acetone for periods of about 3 to 4 minutes. The samples were then washed in Extran MA 02 soap, supplied by Merck Chemicals, and then rinsed several times in deionised water. Finally the samples were rinsed in methanol in an ultrasonic bath several times to remove excess water on the sample surface. A sequence of ultrasonic agitation in acetone, then deionised water and then methanol was used to degrease the rectangular samples and remove physical contaminants from the surface.

5.3 Annealing of samples

The samples were placed inside a small graphite crucible and annealed in a computer controlled high temperature air cooled vacuum Webb® graphite furnace. The oven heats up at a rate of 20°C per minute and the temperature is controlled by a Eurotherm 2704 controller that is linked to a thermocouple and a pyrometer [Web06]. The thermocouple measures the temperature up to 1475°C and the pyrometer takes over at temperatures

above 1525°C. Within the 1475°C-1525°C temperature range, an average value of the pyrometer and the thermocouple is used. A typical heating and cooling curve, which is the temperature curve for an annealing cycle, is shown in Fig. 5.2 and Fig. 5.3.

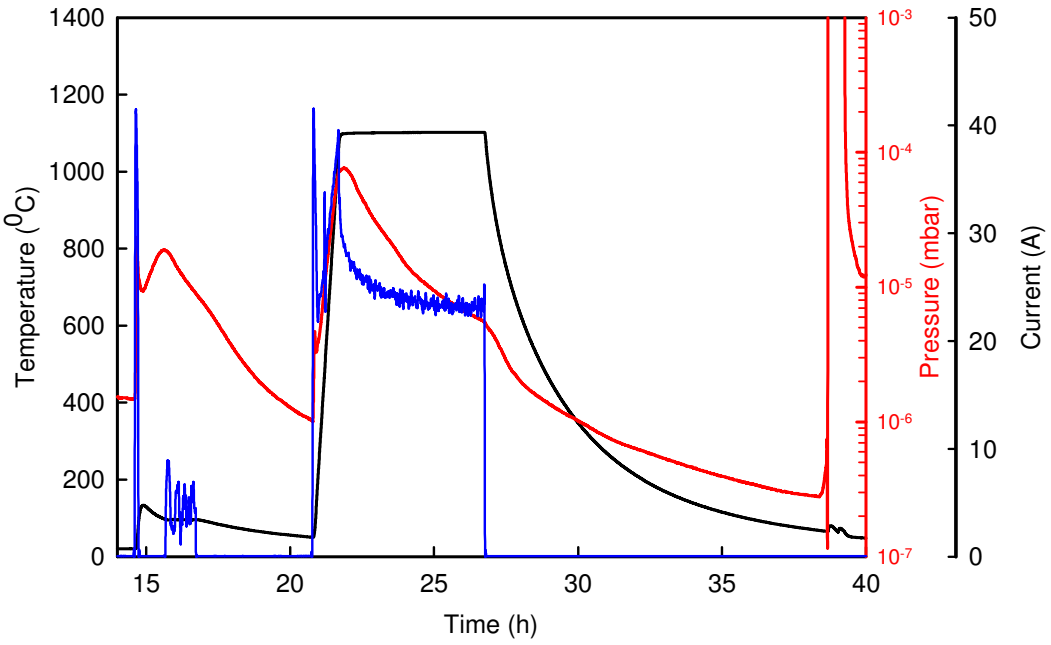

Figure 5.2: Current (blue), vacuum pressure (red) and temperature (black) curves for a 5 hour annealing cycle at 1100°C.

In Fig. 5.2, the temperature curve is represented by the curve in black, the curve in red represents the pressure and the blue one represents the current drawn by the heating element. In order to cut down on the pumping time and to limit the peak pressure during the annealing, a de-gassing exercise was performed. The element was heated to approximately 100°C to facilitate the desorption of water vapour and other gases adsorbed on the fibrous high temperature carbon insulation in the oven. This de-gassing phase is shown by the region from about 0 to 20 hours. In this region, the pressure initially increases from the lower 10^{-5} mbar range and peaks just below 10^{-4} mbar range. This is due the fact that initially, the rate of de-gassing is higher than the pumping rate. The pressure then falls and reaches a minimum in the order of 10^{-6}mbar after pumping for approximately 20 hours.

A current is then supplied to the heating element and the element is allowed to heat up a rate set at 20°C per minute. Fig. 5.3 shows the shape of the heating curve. The current was switched on after almost 21 hours of pumping down the vacuum. This can be seen from the sharp peak in the current curve at this stage before regulation of the current takes place in order to maintain the temperature at the desired levels. The desired annealing temperature of 1100°C is realised in about 55 minutes due to the preset heating rate of 20°C per minute. At this stage, the pressure initially increases due to the significantly higher temperature which results from an increase in the rate of de-gassing. As the annealing proceeds, the pressure decreases again to below 10^{-5} mbar when the pumping rate becomes larger than the rate of de-gassing. The annealing time is then recorded for the period the thermocouple is registering this reading of 1100°C. After 5 hours, the current is switched off and the oven allowed to cool down. The cooling curve is exponential. After a period of about 12 hours when the sample has cooled down to about 40°C, argon gas was let into the furnace to break the vacuum. A corresponding rise in pressure to atmospheric pressure levels can be seen in Fig. 5.2 at this stage. When the sample is removed from the furnace, the chamber was flooded with argon gas to limit the absorption of water vapour as well as other atmospheric gases.

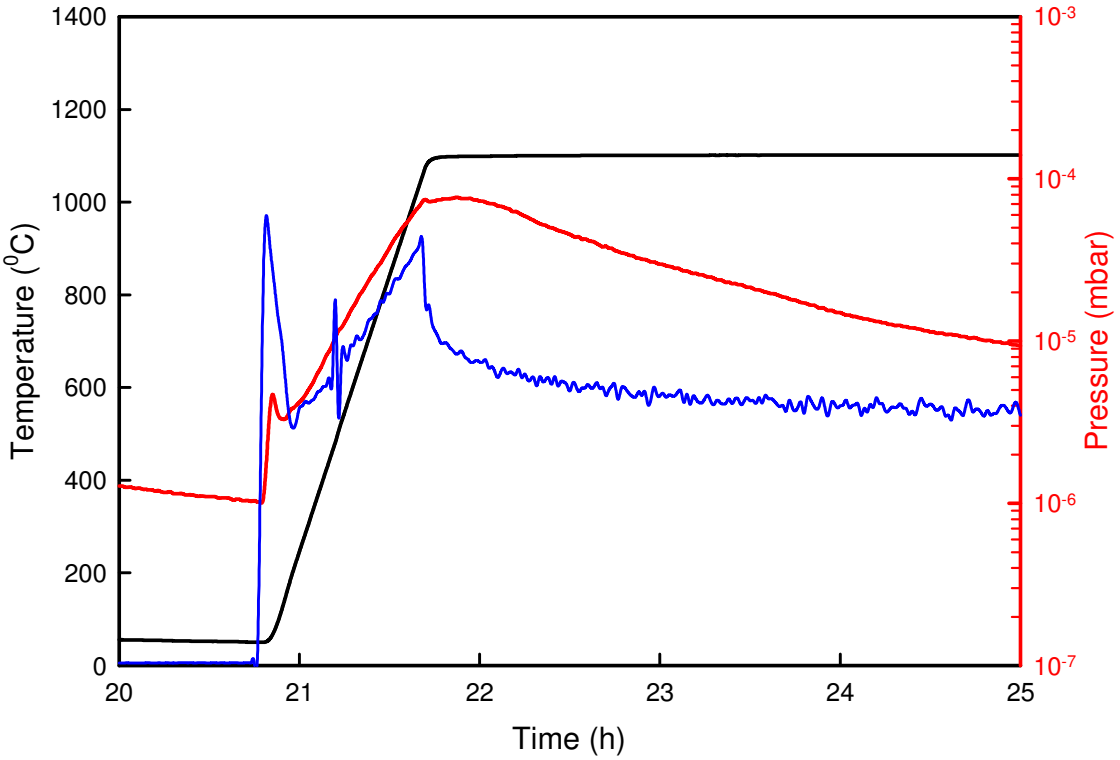

Figure 5.3: Heating curve of the Webb® furnace set to heat up at a rate 20°C per minute.

5.4 RBS experimental set up

In order to perform a backscattering experiment, one has to first produce ions of the desired species. The next step is then to accelerate the ions. The ion beam is then energy analysed by an electromagnet to filter out any unwanted species in the beam. The analysed ion beam is then made to impinge on a target. Some of the backscattered ions are then detected at a prescribed backscattering angle and finally the energy of the detected particles and corresponding data is stored in an appropriate storage system. The setup of the Van der Graaff accelerator of the Department of Physics, University of Pretoria is shown in Fig. 5.4. Fig.5.5 shows a schematic of the accelerator tank. The accelerator tank houses the ion source, charging belt, accelerator tube and the components providing the electrostatic environment of the accelerator. The tank is filled with dry insulating gases like a mixture of N_2 and CO_2 or SF6. A schematic of an R.F

ion source similar to the one used to generate ions in the van der Graaff accelerator of the University of Pretoria is shown in Fig. 5.6. The set up of the energy spectrometry system is shown in Fig. 5.7. A concise description of the physics of the Van der Graaff accelerator and the energy backscattering spectrometry system can be found in the book by Tesmer and Nastasi [Tes95].

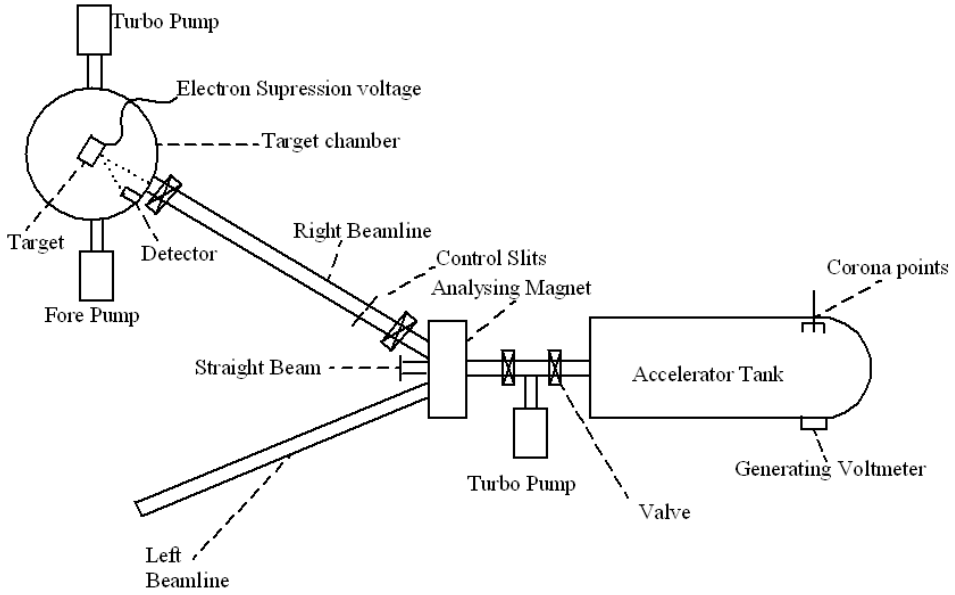

Figure 5.4: Schematic of the Van der Graaff accelerator of the University of Pretoria and its set up for RBS.

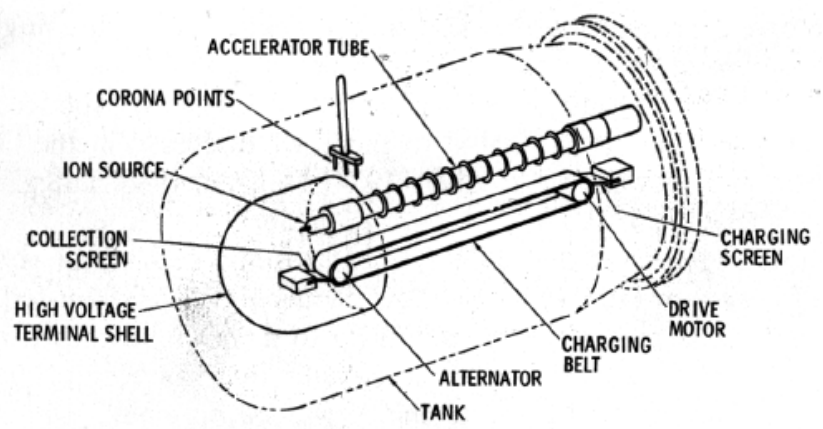

Figure 5.5 Schematic of a Van der Graaff accelerator. Taken from [Chu78]

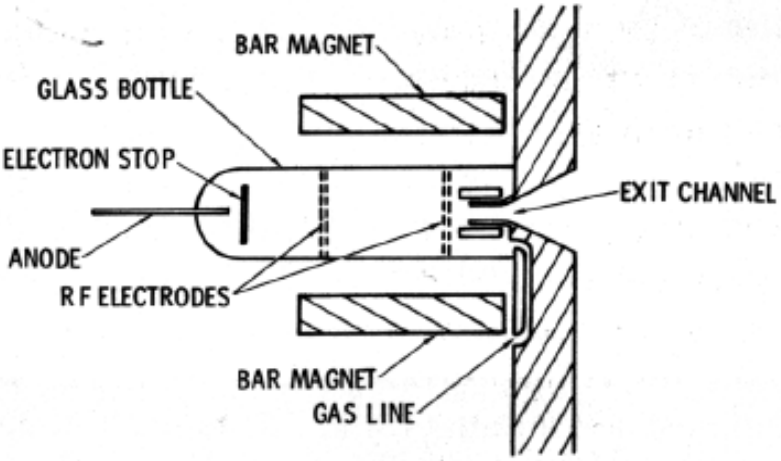

Figure 5.6 Schematic of an rf ion source. Taken from [Chu78]

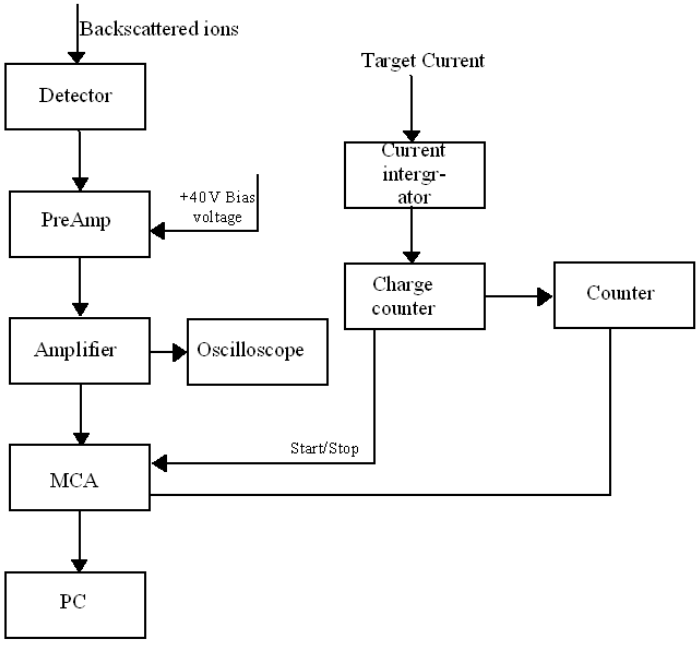

Figure 5.7: Block diagram of the energy spectrometry system used at the University of Pretoria.

5.5 Data acquisition

The electronic set up of the University of Pretoria RBS system is shown in Fig. 5.7. The backscattered α-particles are detected by a Canberra passivated implanted planar (PIPS), partially depleted (PD) surface barrier detector with an active area of 25mm^2 located at an angle of 165° relative to the incident beam. An output charge signal from the detector, which is proportional to the energy of the backscattered particle, is fed into a Canberra 220 pre-amplifier. A +40V bias voltage from a Canberra 3102D high voltage supply is supplied to the detector. In pre-amplifier the charge signal is converted into a voltage signal proportional to the backscattered energy. This voltage signal is then further amplified by a Tennelec TC 243 amplifier. From this main amplifier, a bipolar output signal is fed to an oscilloscope to monitor the shape of the output pulses. Meanwhile, a

unipolar output signal from this main spectroscopy amplifier is fed to the input of a multichannel analyser (MCA).

A current is simultaneously collected at the back of the target and delivered to an Ortec 439 current integrator. A logic signal from the current integrator is responsible for initiation and termination of signal processing by both the MCA and the counter. A desired energy range can be selectively processed by adjusting the lower and upper energy discriminators in the MCA. The sample orientation can be varied during the experiment by making use of a manually controlled precision three axis goniometer. This goniometer is used extensively in the channelling experiments. The use of the goniometer in channelling experiments is outlined in channelling section of chapter 4, in section 4.6.

5.6 Data Analysis

The backscattering energy spectra of counts against channel number were obtained by collecting a charge of 8 μC constituting a run. In order to obtain the energy per channel calibration of the system, backscattering spectra were obtained for runs at three energies. These energies were 1.8 MeV, 1.6 MeV and 1.4 MeV. The positions of channel number of the silicon edge at the different energies were plotted against the corresponding energies. The slope of this plot gives the energy calibration of the system in keV/channel. This energy calibration in keV/channel was then converted into a depth scale calibration in nm/channel, using the computer code A-STOP2 [Fri09]. As stated in chapter 4, the code A-STOP2 uses the energy loss data of Ziegler [Zie77].

The moments R_p, the projected range, and σ, the range straggling or standard deviation of the iodine peak were obtained by fitting the resulting spectra of counts against depth (nm) with the computer program GENPLOT using a Gaussian function. The standard deviation,σ, can be related to the full width at half maximum (FWHM) [Chu78], of a Gaussian distribution by

$$\text{FHWM} = 2(2\ln 2)^{1/2} \times \sigma \tag{5.1}$$

In this study, the FWHM's of the depth profiles after iso-thermal annealing were fitted to the function

$$[W(t)]^2 = 4Dt\ln(2) + [W(0)]^2 \tag{5.2}$$

to obtain *D*.

References

[Chu78] W.K. Chu, J.W. Meyer and M.A. Nicolet, "Backscattering Spectrometry", Academic Press, New York, 1978, p.140

[Fri09] E. Friedland, "A-Stop2" Department of Physics, University of Pretoria, 2009. Private Communication.

[Tes95] J. Tesmer and M. Nastasi, "Handbook of modern ion beam materials analysis", Materials Research Society, Pittsburg, 1995

[Web06] R. D. Webb Company, operating manual, Webb 77. 2006.

[www2] http//:www.cree.com, Mat-catalogue 00M, Cree inc® (06-10-2009).

[Zie77] J.F. Ziegler, "Helium Stopping Powers and Ranges in All Elements", Pergamon Press, New York, 1977.

Chapter 6: Results and Discussion

6.1 The As-Implanted Random and aligned Spectra

The diffusion behaviour of iodine implanted 6H-SiC was investigated with Rutherford backscattering spectroscopy as outlined in chapter 5. A typical RBS spectrum illustrating the random and aligned spectra of iodine implanted 6H-SiC is shown in fig.6.1. The spectrum from the virgin (un-implanted 6H-SiC) is also shown. The α-particle energy employed for the RBS in both the conventional (random) and channeling mode was 1.6 MeV, and the backscattering angle was 165°C. The arrows indicate the signals originating from the surfaces of the corresponding elements in the spectra, that is the iodine surface position, silicon surface, and carbon surface. The signal originating from the surface of each element in an RBS spectrum is defined by the kinematic factor of the element and the α-particle energy.

A backscattered particle has its highest possible energy if the backscattering event occurred at the surface and thus this high energy edge is given by $K_X E_0$, where E_0 is the incident energy of the α-particle and K_X is the kinematic factor of the corresponding element. The kinematic factor therefore gives the position of the edge of each element. The elements with the larger kinematic factors therefore appear at the higher energies in the RBS spectrum. This explains the position of the elements in fig 6.1. Iodine, which is the heavier element of the three, appears in the high energy region of the spectrum, with its edge at channel number 369, followed by silicon, channel number 236 and then the carbon, channel number 102. The kinematic factor is influenced by mass M_2 of the target atom as can be seen from the ideal backscattering case (where θ = 180°) and the kinematic factor given in section 4.2 by equation (4.3) reduces to:

$$K_X = \left[\frac{(M_2 - M_1)}{(M_2 - M_1)}\right]^2 \qquad (6.1)$$

where M_1 and M_2 are the masses of the projectile and target atom respectively.

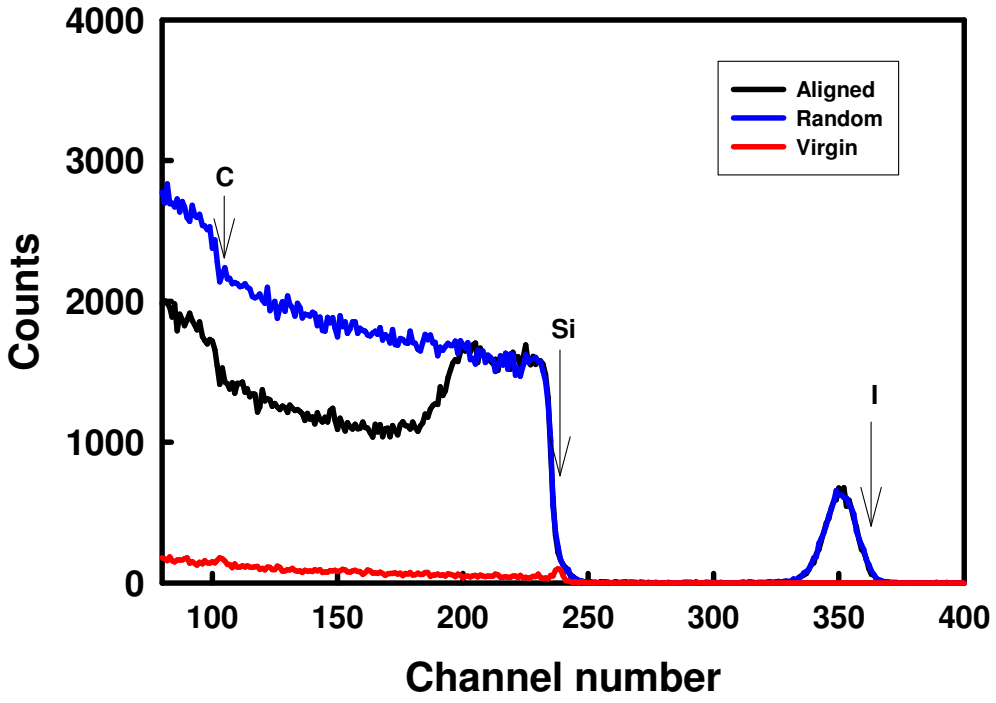

Figure 6.1: Random and aligned backscattering spectra of 6H-SiC implanted at room temperature with $^{127}I^{+}$ ions to a fluence of 1 x10^{16} cm^{-2}. The α-particle energy was 1.6 MeV and a scattering angle of 165° was used. The arrows indicate the high energy edge of each element.

Iodine distribution shown in the spectrum in Fig. 6.1 is approximately Gaussian due to the statistical nature of the implantation process. Identical particles in the ion beam of the species being implanted, in this case, iodine, initially having the same velocity will not necessarily have the same energy after traversing the same thickness in a homogenous target. The resulting statistical uncertainty in the energy of particles penetrating a solid, leads to a statistical distribution in both the number and size of events for a certain depth of penetration.

In Fig. 6.1, the aligned spectrum initially reaches the random spectrum from the silicon edge to around channel 202 showing the presence of an amorphous layer in the near surface region produced as a result of the damage caused by implantation. In the energy spectra shown in Fig. 6.1, a marked decrease in the backscattered yield of the aligned spectrum is observed starting from around channel number 202 down to channel number 188. The range from channel 236 (silicon edge) to channel 188 represents the width of the amorphous region. Beyond this region is the crystalline 6H-SiC not affected by the ion implantation and this can be deduced from the corresponding decrease in the backscattering yield in this region. The yield in the region behind the damaged peak is higher than that of the virgin (un-implanted) crystal due to the dechanneled fraction of α-particles in the disordered region. The increase in yield observed after the minimum yield towards the lower energy region of the spectra can be understood from the differential cross-section. As outlined in section 4.1, the differential cross-section is inversely proportional to the square of the energy, $d\sigma/d\Omega \propto E^{-2}$ and therefore backscattering yield increases sharply with decreasing energy.

The iodine implantation profile obtained experimentally with RBS is presented in Fig. 6.2 along with a simulation of the profile calculated by the TRIM-98 code [Zie85]. The profiles are plotted showing the variation of the relative atomic density of the implanted iodine with depth. This atomic density, expressed as a percentage, gives a measure of the concentration of the iodine at a specific depth. In this study, the density of SiC was taken as 3.21 gcm^{-3} which is equivalent to 9.641×10^{22} atoms/cm^3 and therefore relative atomic density quantifies how many atoms of iodine are present at a certain depth. In this simulation, the displacement energies of the carbon and silicon were assumed to be approximately 21eV and 35eV respectively [Dev00]. The theoretical prediction of the projected range, R_p, was approximately 100 nm, while the projected range as observed experimentally was around 95 nm. There is reasonable agreement between the two values shown by a difference of only 5%. The range straggling,σ, however, is about 30% larger in experimental profile than in the simulation. In the TRIM-98 code, the target is considered to be amorphous with atoms at random locations. The directional properties of the crystal lattice are ignored. Other reasons for the differences in the profiles arise

from the numerous approximations made by TRIM [Zie85]. Some of the approximations made by TRIM are:

- The interactions are taken as binary collision where the influence of neighbouring atoms is neglected.
- The recombination of knocked out atoms with vacancies is neglected.
- The electronic stopping power is an averaging fit to a large number of experiments.
- The interatomic potential is taken as a universal form which is an averaging fit to quantum mechanical calculations.

For the other moments, the kurtosis (β = 3.1) and skewness (γ = 0.2), the implanted iodine profile is found to be nearly Gaussian. For a Gaussian distribution, β = 3 and γ = 0. In obtaining the simulation, the parameters used such as the fluence, were identical to the ones for the experimental conditions. With the integrals of the resulting profiles being equal, the broader profile of the experimental sees its peak height being lower than the one obtained by the TRIM simulation.

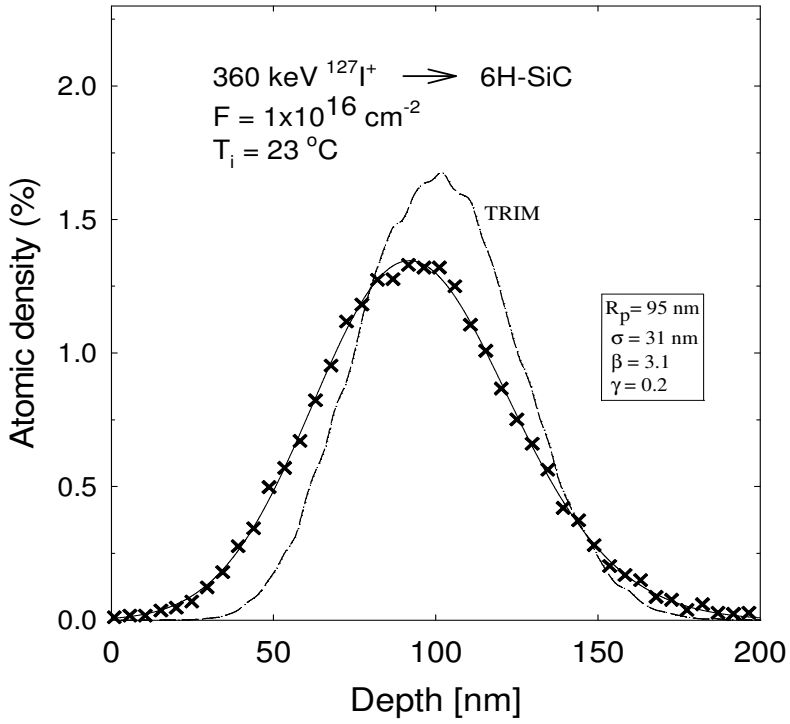

Figure 6.2: RBS iodine depth profile in 6H-SiC, (curve with crosses), along with the theoretical distribution obtained with the TRIM-98 code (plain curve) [Zie85].

6.2 Initial Isochronal Annealing Results

6.2.1 Radiation Damage Results

Following a depth conversion as described in section 4.3, the aligned and random spectra of the initial iodine implanted SiC compared with the aligned spectra for the 5 hour isochronal annealing cycles at 1000°C, 1200°C and 1300°C are shown Fig. 6.3. The aligned spectra are all normalised to the random spectrum.

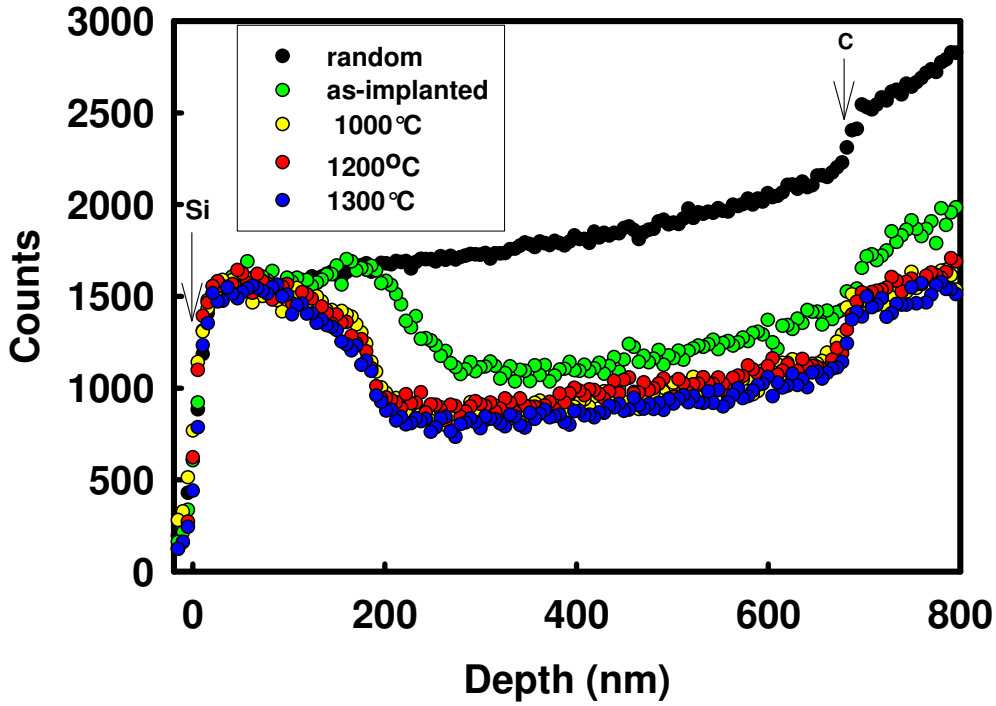

Figure 6.3: Random and aligned backscattering spectra of 6H-SiC implanted at room temperature with 360 keV $^{127}I^{+}$ ions to a fluence of 1×10^{16} cm^{-2} and subjected to isochronal annealing for 5 hours at 1000°C, 1200°C and 1300°C. The α-particle energy was 1.6 MeV and a scattering angle of 165° was used.

Analysis of the as-implanted sample reveals that the aligned spectrum reaches the random yield level from the surface up to a depth of about 260 nm. This region can be described as highly disordered or amorphised. This result is in agreement with results by Wendler *et al*, [Wen98] Audren *et al*, [Aud08] and McHargue *et al*,[McH93], who in their studies of SiC found that SiC is easily amorphised by ion implantation at room temperature. By implanting iodine at 700 keV up to a fluence of 2.7 x 10^{14} cm^{-2} in SiC at room temperature, Audren *et al*, observed that the damage produced, resulted in an amorphous region extending from the surface to a depth of approximately 250 nm.

After sequentially annealing the sample isochronally for 5 hour cycles, appreciable recystallisation from the crystalline bulk-damaged region interface was observed after the

5 hour cycle at 1000°C. This can be seen from the separation of the damaged peak from the random level. The damage peak which initially extended from the surface to a depth of approximately 260 nm only reaches the random level up to a depth of 100 nm. This behavior shows this previously amorphised region now exhibits some sort of long range order that is, some recystallisation has occurred. Similar results were observed by Audren *et al*, [Aud08]. The fact that this recystallisation takes place from the interface region suggests that the recystallisation is epitaxial. Investigations by Pacaud *et al*, [Pac96] and Wendler *et al*, [Wen98] also suggest that the onset of this epitaxial recystallisation in SiC is around 1000°C.

The annealing cycle at 1000°C for 5 hours sees the width of the damaged region being reduced to about 220 nm. Subsequent annealing cycles at 1200°C and 1300°C, again for 5 hours each, results in the width of the amorphous region being reduced to about 200nm and 190 nm respectively. As described in section 4.4, the spectrum of a compound sample is a superposition of the spectra generated by each of the constituent elements. In Fig. 6.3, all of carbon's contribution to the spectrum is added to the low energy region of silicon. It for this reason that our discussion on radiation damage is focusing only on the silicon part of the spectrum as the carbon edge is not clearly resolved in the spectrum shown in Fig. 6.3.

6.3 Iodine Distribution Profile Behaviour

6.3.1 Sequential Isochronal Annealing Experiments

The as-implanted iodine profile can be described by a near Gaussian distribution. Thermal annealing up to a temperature of 1000°C for 5 hours does not produce any noticeable change in the iodine distribution profile. This result is illustrated in Fig. 6.4. We conclude that we do not detect any diffusion of the iodine at this temperature and annealing time. Audren *et al*, [Aud08], also reported that they could not detect any diffusion of the iodine up to an annealing temperature of 1000°C for 30 minutes.

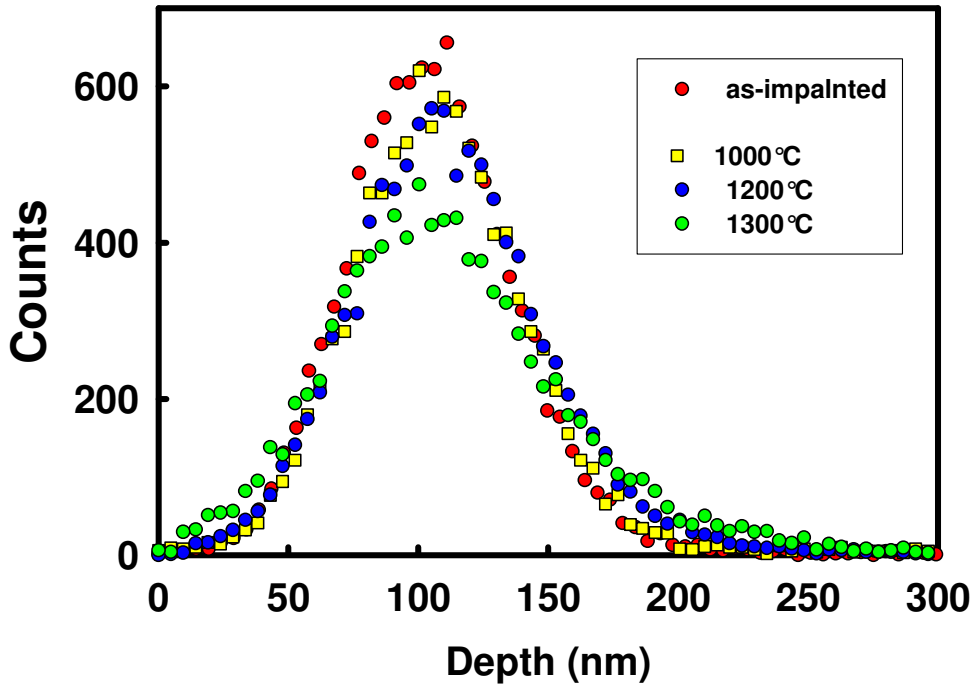

Figure 6.4: Iodine as-implanted depth profile along with profiles of the isochronally annealed profiles at 1000°C, 1200°C and 1300°C. The annealing time was 5 hours at each stage.

Subsequent anneals, at 1200°C and 1300°C, again for 5 hour cycles, were performed and broadening of the iodine profile was observed for both annealing cycles. This is illustrated by the change in the FWHM of the profiles as shown in Table 6.1. After annealing at 1200°C, the FWHM of the iodine profile increases to (84 ± 2 nm) and then to (94 ± 2 nm) after 1300°C from an initial (72 ± 1 nm). This result seemed to suggest that the iodine starts to diffuse at a temperature of around 1200°C.

In the RBS spectrum, the amount of iodine is proportional to the area under the iodine distribution curve. By comparing the integrals of the peaks, approximately 10% of the iodine is lost through the front surface after the 1300°C, 5 hour annealing cycle.

Table 6.1: Values of the FWHM and peak integral of the iodine profile for the isochronal annealing cycle.

Annealing Temperature(°C)	FWHM (nm)	Peak Integral (Counts)
Room temperature	72 ± 1	10 313 ± 102
1000	75 ± 2	9 798 ± 99
1200	84 ± 2	9 761 ± 99
1300	94 ± 2	9 365 ± 97

6.3.2 Isothermal Annealing Results

Isothermal annealing of fresh iodine room temperature implanted samples were then performed. We decided to start annealing at a temperature of 1200°C based on the results of the preliminary isochronal annealing experiments where the broadening of the of the iodine peak was observed in the 1200°C-1300°C temperature range. The iodine profiles after some isothermal annealing at 1200°C up to a total annealing time of 60 hours, were compared with the as-implanted profile are shown in Fig 6.5.

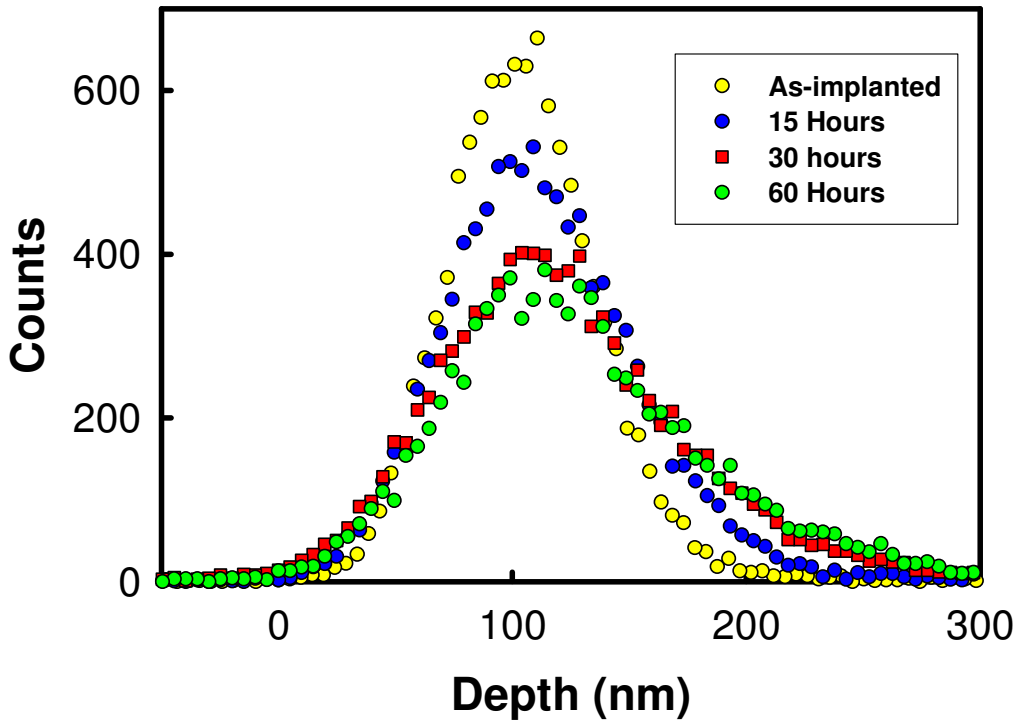

Figure 6.5: Iodine depth profiles of 6H-SiC implanted at room temperature after annealing isothermally at 1200°C for 15, 30 and 60 hours.

After annealing for a period of 15 hours, and fitting the iodine profile to a Gaussian function as described in chapter 5, significant broadening of the iodine profile was observed. After 5 hours of annealing, the FWHM of the iodine profile is approximately (84 ± 2 nm), up from the initial (72 ± 1 nm) of the as implanted profile. This broadening suggests that the iodine is already diffusing in the 6H-SiC at this temperature. From the profile, the iodine appears to be diffusing into the bulk and towards the surface. There is some loss of iodine at the front surface observed after annealing for a period of 15 hours (about 4%). On annealing the sample for another cycle, up to a total of 60 hours, further broadening of the profile is noted with the FWHM increasing to (155 ± 3 nm). The iodine moves deeper into the bulk and also moving towards the surface. Approximately 15% iodine was lost after 60 hours of annealing after comparing the integrals of the iodine profiles. The profiles become increasingly asymmetric with annealing time. Due to the asymmetric nature of the profiles of the longer annealing times, the fitting of the curves

was performed using only the experimental data extending from the projected range into the bulk.

Table 6.2: Values of the FWHM and peak integrals of the iodine profile for the isothermal annealing series at 1200°C

Annealing Time(Hours)	FWHM(nm)	Peak Integral (Counts)
As-implanted	72 ± 1	10 160 ± 101
5	84 ± 2	9 897 ± 99
15	90 ± 2	9 815 ± 99
30	113 ± 3	9 726 ± 99
60	155 ± 3	8 529 ± 92

After realising that annealing at 1200°C induces appreciable broadening of the iodine profile with annealing time, another isothermal annealing series at a lower temperature of 1100°C was performed. Fitting the iodine profiles to a Gaussian revealed no change in the iodine profiles up to an annealing time of 30 hours. Thus no diffusion of the iodine could be detected by our system at 1100°C for 30 hours. A hint of the profile broadening was observed after 60 hours with no loss of iodine observed. Thus iodine transport at this temperature is very low and could barely be detected by our system. In this case the profiles remained symmetrical.

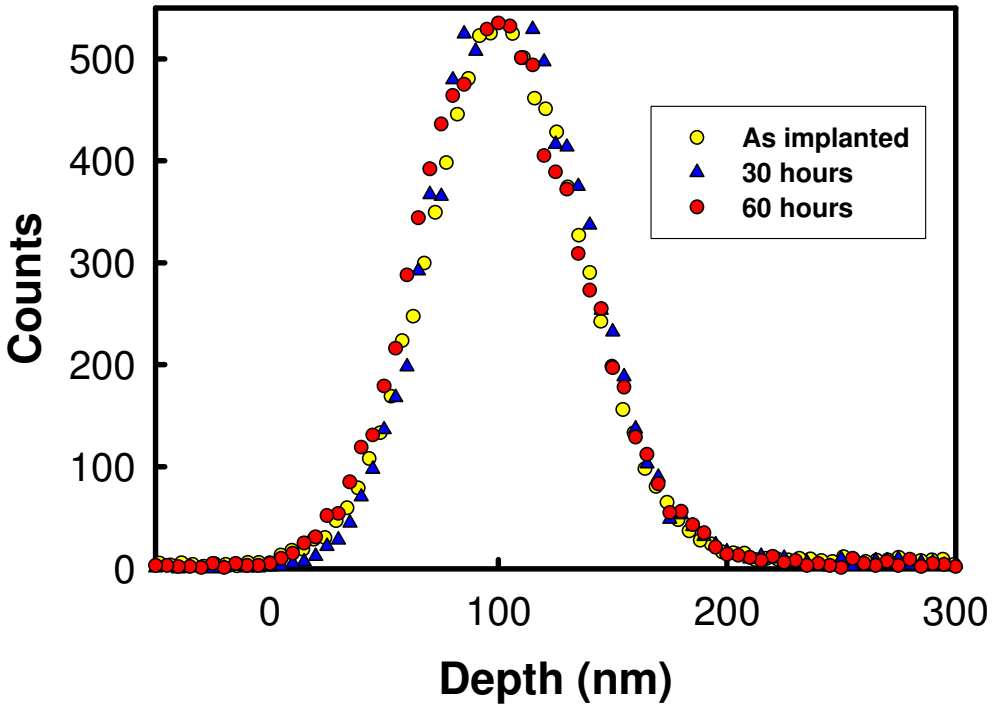

Figure 6.6: Iodine depth profiles of 6H-SiC implanted at room temperature after annealing isothermally at 1100°C for 30 and 60 hours.

Table 6.3: Values of FWHM and peak integrals of the iodine profile for the isothermal annealing series at 1100°C

Annealing Time(Hours)	FWHM(nm)	Peak Integral (Counts)
As-implanted	81 ± 1	10 284 ± 101
5	80 ± 1	10 181 ± 101
30	82 ± 1	9 779 ± 99
60	89 ± 2	9537 ± 98

As discussed in chapter 2, section 2.2, the diffusion coefficient D, can be extracted from the slope of a plot of the squares of the FWHM of the iodine profiles as a function of

annealing time. The squares of the FWHM as a function of annealing time for temperatures 1100°C and 1200°C are shown in Fig. 6.7.

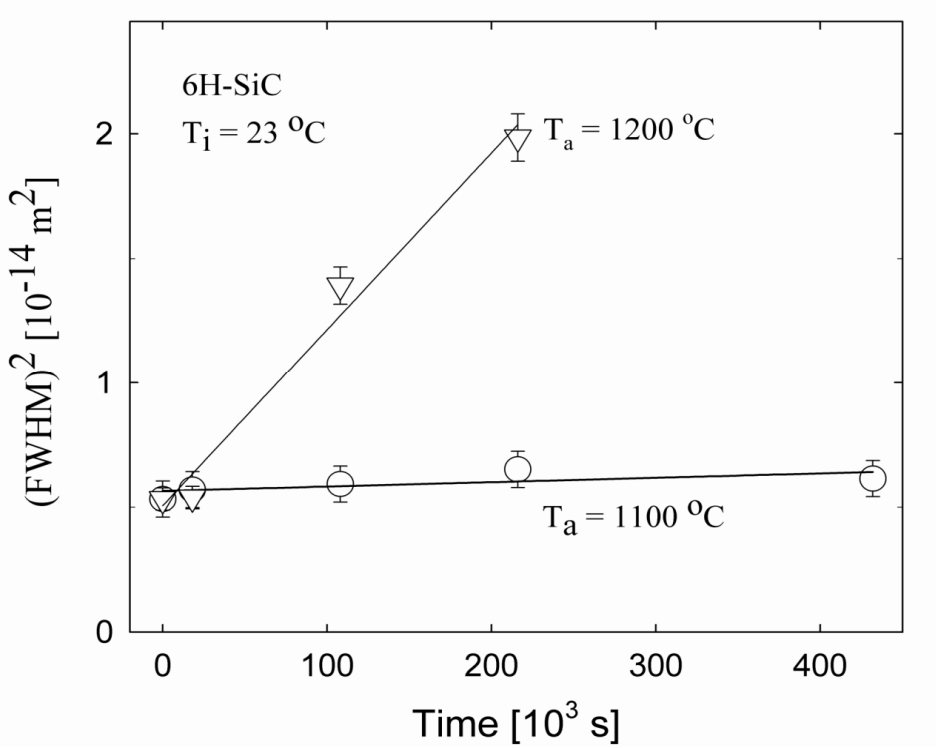

Figure 6.7: Squares of iodine profile widths (FWHM) as a function of isothermal annealing time in 6H-SiC for T_a = 1100°C and T_a = 1200°C.

From the slopes of the isothermal annealing curves in Fig. 6.7, the diffusion coefficients were found to be approximately $(0.6 \pm 0.4) \times 10^{-21}$ m^2 s^{-1} and $(2.5 \pm 0.3) \times 10^{-20}$ m^2 s^{-1} at 1100°C and 1200°C respectively. At 1100°C, the error is in the order of the value of the diffusion coefficient. This suggests that this could be the detection limit of our system. Any diffusion taking place at this temperature and at temperatures below 1100°C cannot be detected by our RBS set up. This result is comparable to that obtained by Audren et al, [Aud98]. Their work showed that iodine transport in 6H-SiC could not be detected even after annealing up to a temperature of 1000°C. The case of iodine's low mobility in SiC at 1100°C was augmented further by taking into consideration, the diffusion coefficient extracted from the isothermal annealing series $(0.6 \pm 0.4) \times 10^{-21}$ m^2 s^{-1} , and solving the diffusion equation numerically using the program DIFFUS 1

[Fre09]. The program DIFFUS 1 uses the finite difference method to solve the diffusion equation numerically. A good account of the finite difference method can be found in the book "The Mathematics of Diffusion" by J. Crank [Cra83]. In this study, we used the program DIFFUS to calculate the fractional release of iodine for D= 10^{-21} $m^2 s^{-1}$ through 35 µm SiC. The results are presented in Fig. 6.8 for an annealing time of one year.

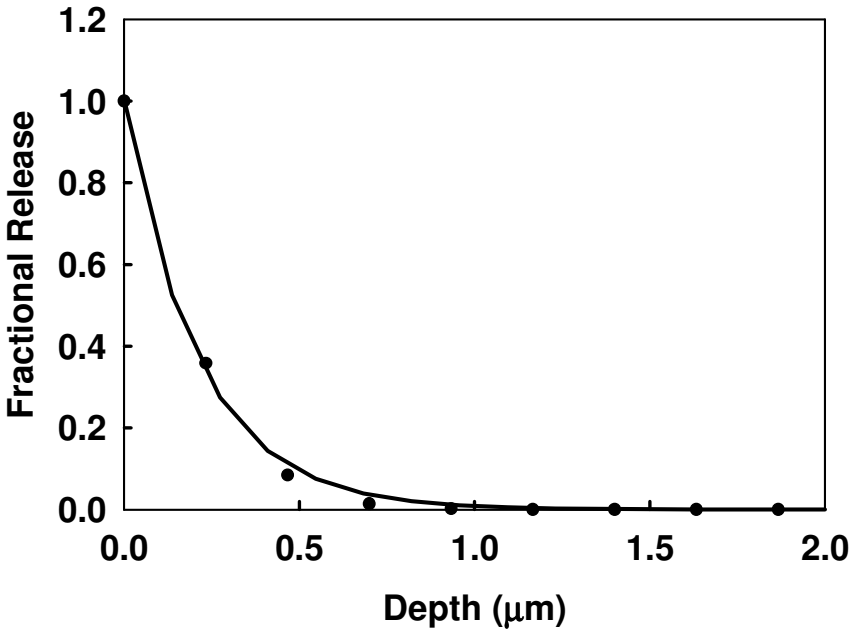

Figure 6.8: Fractional release of iodine from 35 µm SiC for a total annealing time of one year

The iodine concentration was assumed to be 100% at the surface and 0% at a depth of 35 µm. The results presented in Fig. 6.8 show that from the diffusion coefficient extracted at 1100°C, the iodine does not even reach a depth of 2 µm even after annealing for one year.

At 1200°C the diffusion coefficient deduced from the broadening of the profiles is significantly higher with an upper limit of D < 10^{-20} $m^2 s^{-1}$.

Results from the 1100°C isothermal annealing series are certainly encouraging for the use of SiC as an effective barrier in the retention of fission iodine. Any diffusion taking

place at this temperature is below 10^{-21} m^2s^{-1}. SiC can then be regarded as an effective barrier to fission iodine under normal PBMR reactor operating conditions where the average temperature is around 950°C or lower. At 1200°C, the relatively small loss of iodine (around 10%) after a 60 hour anneal, suggests that SiC's ability to retain the fission iodine is quite good. Iodine with a low boiling point of 183°C, should easily evaporate on reaching the silicon carbide surface. The low loss of iodine would suggest that it becomes somehow bound to the lattice atoms. After a 30 hour anneal at a substantially higher temperature of 1500°C, Fig. 6.9, an iodine peak is still detectable by RBS. The apparent high retention of the iodine in SiC could suggest that there could be some compound formation taking place. Previous studies by *Kemerink et al*, [Kem83], suggest that iodine does indeed have some affinity for silicon. In their work, RBS and channeling studies of iodine-implanted silicon show that after oven annealing at 875°C, more than 95% of iodine atoms occupy lattice positions, or near lattice positions. Similar iodine behaviour in SiC could result in compound formation at the higher temperatures employed during our annealing cycles.

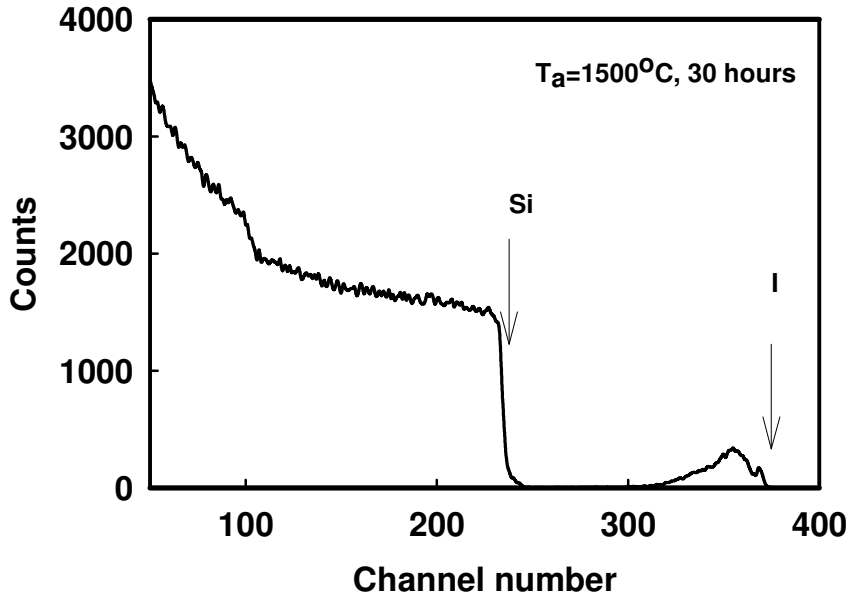

Figure 6.9: Random α- particle backscattering spectrum of iodine implants in 6H-SiC after 30 hours annealing at 1500°C.

References

[Aud08] A. Audren, A. Benyagoub, L. Thome and F. Garrido, Nucl. Instrum. Meth. Phys. B 266 (2008) 2810

[Cra83] J. Crank, "The Mathematics of Diffusion", Oxford University Press, Bristol, 1975, p.141

[Chu78] W. Chu, J. Meyer and M. Nicolet, "Backscattering Spectrometry, Academic Press, New York, 1978

[Dev00] R. Devanathan, W. Weber and F. Gao, Nucl. Mater. 278 (2000) 258

[Fri09] E. Friedland, "DIFFUS 1" Department of Physics, University of Pretoria, 2009. Private communication

[Kem83] G. Kemerink, D. Boerma, H De Waard and L. Niesen, Rad. Effects. 70 (1983) 183

[McH93] C. McHargue and J. Williams, Nucl. Instrum. Meth. Phys. B 80/81 (1993)

[Pac96] Y. Pacaud, J. Stoemenos, G. Brauer, R. Yankov, V. Heera, M. Voelskow, R. Kogler and W. Skorupa, Nucl. Instrum. Meth. Phys. B 120 (1996) 177

[Wen98] E. Wendler, A. Heft and W. Wesch, Nucl. Instrum. Meth. Phys. B 141 (1998) 105

[Zie85] J. Ziegler, J. Biersack and U. Littmark, "The Stopping and Ranges of Ions in Solids", Pergamon Press, New York, 1985

Chapter 7: Conclusion

6H-SiC wafers were implanted with $^{127}I^{+}$ ions at room temperature to a fluence of 1×10^{16} cm^{-2}. Our study shows that implantations at room temperature produce a highly disordered or amorphous region from the surface up to a depth of about 260 nm. At room temperature, the recombination of displaced atoms with vacancies and annealing of radiation damage is inhibited by the low thermal energy of the displaced lattice atoms. The near surface region thus exhibits no long range order. Rutherford backscattering in conjunction with channeling analysis of the isochronally annealed samples reveal that the onset of the recystallisation of the amorphous SiC is around 1000°C. The regrowth appears to be epitaxial. The recystallisation starts from the interface between the crystalline bulk and the damaged region and proceeds towards the surface. This could imply that the regrowth follows the orientation of the underlying crystalline bulk.

Analysis of the iodine depth profiles during the 5 hour isochronal annealing cycles show that the full width at half maximum of the profiles start to broaden at a temperature around 1200°C. This broadening which signifies the spreading of the concentration profile of the implanted iodine indicated that iodine diffuses at 1200°C. In order to extract a diffusion coefficient, isothermal annealing experiments were performed at 1200°C up to an annealing time of 60 hours. Comparison of the FWHM's of the annealed profiles with the as implanted profiles show that the FWHM increases linearly with annealing time at this temperature. The iodine profiles which are initially Gaussian become increasingly asymmetric with annealing time. The iodine appears to diffuse more towards the bulk than towards the front surface. The diffusion coefficient at this temperature was approximately $(2.5 \pm 0.3) \times 10^{-20}$ m^{2} s^{-2}. From the integrals of the iodine profile, iodine loss through the front surface is relatively low at around 15% even after annealing for 60 hours.

From isothermal annealing experiments preformed at a temperature of 1100°C, the broadening of the iodine profile with annealing time is barely detectable by our system up to 60 hours. The extracted diffusion coefficient was approximately $(0.6 \pm 0.4) \times 10^{-21}$ m

^{2} s^{-2}. We conclude that iodine transport in SiC at this temperature is very low. This result is certainly encouraging for the use of SiC as a barrier to fission iodine. In the PBMR, the operating temperature is around 1000°C under normal conditions. RBS analysis of a sample annealed for 30 hours at 1500°C reveals that an iodine peak is still detectable. Given iodine's modest boiling temperature approximately 183°C, we conclude that this low loss of iodine through the front surface points to the formation of a strong bond and possible compound formation between SiC and iodine. Further investigations will need to be carried out to ascertain the possibility of compound formation between iodine and SiC. Given the drastic increase in the diffusion coefficient extracted at 1200°C from the diffusion coefficient obtained at a temperature 100°C lower, studies at intermediate temperatures like 1125°C, 1150°C and 1175°C are planned to give a clearer picture of the diffusion behaviour. Diffusions coefficients at extra annealing temperatures are also needed to determine the activation energy as well as the pre-exponential factor for iodine diffusion in SiC. Diffusion studies of samples implanted at higher temperatures like from 200°C, up to 600°C are also planned to investigate the influence of implantation temperature. RBS and channeling studies will be complemented by several techniques like high resolution Scanning Electron Microscopy (SEM) for surface analysis, Transmission Electron Microscopy and Raman spectroscopy.